Sensorless Control of Synchronous Reluctance Machine

Banuso Abdulquadri Oluwatobi

Supervisor: Professor David Lowther

McGill University

A report submitted to McGill University in partial fulfillment of the requirements for the degree of Master of Engineering

Master's Project

April 2022

Acknowledgment

This project was conducted at the Computational Electromagnetics Lab, Department of Electrical Engineering, McGill University. First, I want to give great gratitude to my supervisor Professor David A. Lowther. His patient instruction, constructive criticism and continuous support accompanied me all the way through this master's project. I am also very thankful to Dr. Sumeet Aphale for introducing me to the beautiful world of Systems theory. I am grateful for having insightful discussions with my colleagues at the Computational Electromagnetics Lab, in particular, Alok Patel. His input on computational modelling and validation of electric machines helped me at different points of this project.
Finally, I am eternally grateful to my family and friends, who always showed me unconditional encouragement and love at every stage of my life. Without all these people, I would not be able to complete this project successfully.

Banuso Abdulquadri Oluwatobi, April 2022

Abstract

This project report focuses on the design and implementation of a Finite Control Set Model Predictive Control (FCS-MPC) of a Synchronous Reluctance Machine (SynRM) to control the rotor speed and the design of the Extended Kalman Filter (EKF) used to observe the machine states in feedback to the control system. The non-linear model of the SynRM is derived based solely on the electrical and mechanical equations without taking magnetic saturation in consideration.

The FCS-MPC uses the discretized model of the SynRM and a multi-objective cost function is introduced to derive the optimal voltage input at the next time step to the machine. The cost function deals with three targets: speed tracking, torque by ampere optimization, smooth behaviour of torque and limitation. The speed tracking and torque by ampere optimization part enables the SynRM to generate the reference I_q current. The limitation part aims to avoid the current states reaching undesired operation regions. A Field Oriented Control (FOC) scheme using cascaded Proportional-Integral controllers has been designed for the benchmark electric drive system.

Simulation results show the robustness and reliability of the proposed control and estimation algorithm for the SynRM. For simplicity, the parameters of the EKF covariance matrices and weighting factors of the FCS-MPC are tuned offline using swarm optimization algorithms. The drive system is implemented in Simulink to demonstrate its feasibility.

Contents

List of Figures

List of Tables

Chapter 1

Introduction

1.1 Motivation

Due to the growing demand for higher efficiency in electrical machines, the Synchronous Reluctance Motor (SynRM) has gained interest in recent years. The SynRM presents a simple, lightweight, and robust design, and the absence of magnets or windings on the rotor means that it generates mainly reluctance torque. SynRM combines the simplicity of an induction machine with the high efficiency and performance of the permanent magnet synchronous motor. It can also be said to be more environmentally and sustainably friendly than the Permanent Magnet motor due to the lack of permanent magnets in its design.
A SynRM is typically controlled using Field Oriented Control (FOC) with cascaded speed and current proportional-integral (PI) controllers with mechanical Hall effect sensors used to measure rotor speed and position of the motor drive in a feedback loop to control the speed or torque of the machine. However, the measurable outputs of the system, the rotor speed and position are not always available due to the high costs of sensors, their weakness and noise sensitivity.
To overcome this difficulty, a robust estimation algorithm is needed to reconstruct unmeasurable states (position and speed). Recent developments for sensorless technologies in the industry have been proposed [1] with different approaches such as Signal Injection, Back electromotive force (EMF) estimation, Stochastic Kalman Filters, Sliding Mode Observers, and Neural Networks methods to estimate the rotor position and speed. To achieve high-performance objectives, the design of

robust controllers requires suitable models describing the dynamical behaviour of the machines. The Finite Control Set Model Predictive Controller (FCS-MPC), whose core is based on integer optimization, is proposed in [2]. The control structure is capable of handling system objectives and constraints like voltage tracking, torque per ampere optimization, and minimization of switching losses in a systematic way.
Due to recent technological advances in power electronics and signal processing fields, complex control like the FCS-MPC and estimation strategies like the stochastic Kalman Filter can be implemented using Digital Signal Controllers to accomplish different objectives in varying operating regions.

1.2 Goal

In this report, the goal is to develop a framework called sensorless FCS-MPC that can realize good control of the electric drive system over a wide speed range, while a sensorless FOC with cascaded PI control will serve as a reference.
In detail, the performance of the FCS-MPC and observer (estimation algorithm) is evaluated by reference speed and current tracking and torque quality compared to those which occur when using the PI control scheme as a benchmark. Also, the impact of high frequency injection signals for estimating the rotor position and speed in the low speed region is analyzed.

1.3 Outline

Chapter 2 introduces the theoretical knowledge of the SynRM, 3 phase two-level voltage source inverter (VSI), and space vector pulse width modulation (SVPWM) in the electric drive system. A non-linear SynRM model is derived, and a brief literature review of existing control strategies and estimation strategies are discussed to realize the control of a SynRM under different operating conditions. Chapter 3 focuses on the execution of the FCS-MPC algorithm, a discretized model of the SynRM is utilized in the FCS-MPC to help predict the system states, and find the optimal voltage input. Later parts of chapter 3 introduce the use of the nonlinear dynamic model of a SynRM in the design of the extended Kalman Filter (EKF).

Chapter 4 demonstrates the simulation study, the main system parameters used for the simulation are listed, and the operation performances between the FCS-MPC and FOC as well as the operation performances between different FCS-MPC configurations are compared. In Chapter 5, conclusions of this report are drawn and future work is proposed.

Chapter 2

Background

2.1 Introduction of the Synchronous Reluctance Machine

The Synchronous Reluctance Machine (SynRM) has been gaining momentum due to growing demands for higher energy efficiency in the industry. It presents a simple structure, lightweight with mechanical robustness, and an absence of windings or magnets in its rotor which is made of only ferromagnetic material. When compared to the Induction Machine (IM), the SynRM has higher energy efficiency, lower losses due to the absence of the rotor circuit, and has a relatively low production cost, and the production of mainly reluctance torque makes it an attractive option for variable speed drives. An advantage of the SynRM, when compared to Permanent Magnet Synchronous Machines, is the absence of permanent magnets, which are commonly made of rare earth materials that are geographically restricted and depending on price trends can be expensive.
There are different rotor topologies of the reluctance machine presented in figure 2.1. This report deals with a simple salient pole SynRM with its associated electrical and mechanical parameters.

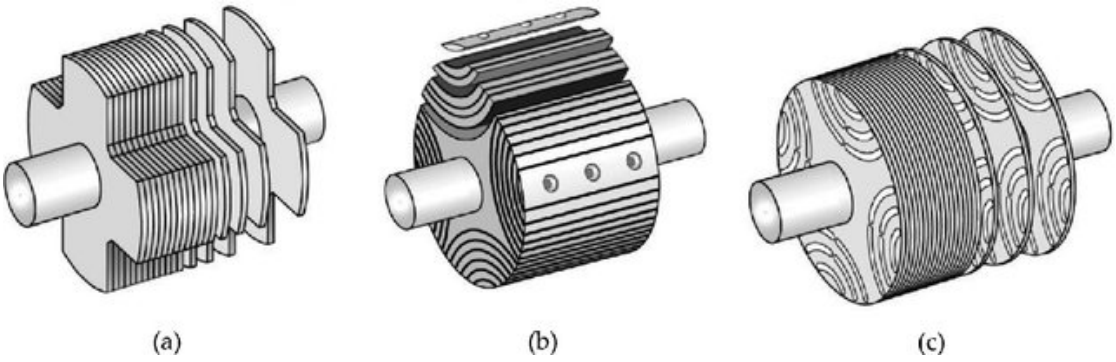

Figure 2.1: SynRM Rotor Topologies: (a) simple salient pole, (b) axially laminated anisotropic rotor, and (c) transversally laminated anisotropic rotor

2.1.1 Common coordinate systems for the analysis of SynRM

There are three commonly used coordinate systems for the modeling and analysis of the dynamic performance of electrical machines. Figure 2.2 shows the relations between the different coordinate systems.

1. abc three-phase stationary coordinate system: The three-phase windings are spatially located on the a,b, and c axes respectively. The stator electrical vector components such as voltage, current, and flux hold their actual values on these axes. The rotor flux ψ_e rotates counter-clockwise in this coordinate system and the electrical speed ω_e is positive.

2. $\alpha\beta$ two-phase stationary coordinate system: The α-axis is aligned with the phase a axis of the three-phase abc system, the β-axis is 90deg in advance of the α-axis. The rotor flux r rotates counter-clockwise in this coordinate system and the electrical speed ω_e is positive.

3. dq two-phase rotating coordinate system: The orientation of the d-axis is aligned with the rotor flux ψ_e, the q-axis is 90deg in advance. The dq coordinate system rotates counter-clockwise along the $\alpha\beta$ coordinate system with the same electrical speed ω_e of the rotor flux ψ_e, the electrical rotor angle θ_e is defined as the angle between the α-axis and the d-axis. The dq two-phase rotating coordinate system helps in simplifying the analysis of the SynRM since in this coordinate system, the electrical vector components are

DC quantities. A standard control system can be designed and implemented under this pre-condition.

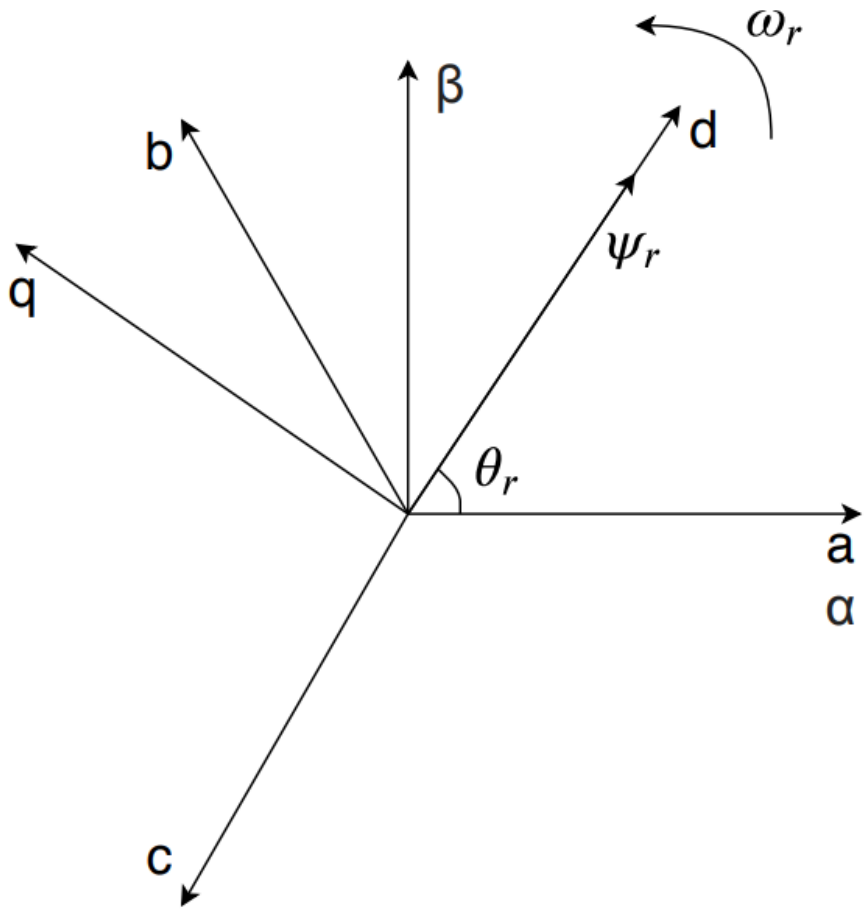

Figure 2.2: Relation between the three commonly used coordinate systems

There are two commonly used choices of coordinate system transformation, an amplitude invariant transformation and a power invariant transformation. The transformation functions are listed below.

2.1.1.1 Transformation between the abc and $\alpha\beta$ coordinate systems (Clarke transformation)

If three stator windings are completely symmetrical, the zero-vectors can be neglected, i.e., $x_a + x_b + x_c = 0$. Thus the transformation between the abc and $\alpha\beta$

coordinate systems can be simplified from the Clarke transformation as:

$$\begin{bmatrix} x_\alpha \\ x_\beta \end{bmatrix} = C_{3s/2s} \begin{bmatrix} 1 & -\frac{1}{2} & -\frac{1}{2} \\ 0 & \frac{\sqrt{3}}{2} & -\frac{\sqrt{3}}{2} \end{bmatrix} \begin{bmatrix} x_a \\ x_b \\ x_c \end{bmatrix} \tag{2.1}$$

$$\begin{bmatrix} x_a \\ x_b \\ x_c \end{bmatrix} = C_{2s/3s} \begin{bmatrix} 1 & 0 \\ -\frac{1}{2} & \frac{\sqrt{3}}{2} \\ -\frac{1}{2} & -\frac{\sqrt{3}}{2} \end{bmatrix} \begin{bmatrix} x_\alpha \\ x_\beta \end{bmatrix} \tag{2.2}$$

For the power invariant transformation, $C_{3s/2s} = \sqrt{\frac{2}{3}}$, $C_{2s/3s} = \sqrt{\frac{2}{3}}$. For the amplitude invariant transformation, $C_{3s/2s} = \frac{2}{3}$ and $C_{2s/3s} = 1$

2.1.1.2 Transformation between the $\alpha\beta$ and dq coordinate systems (Clarke - Park transformation)

Since the dq coordinate system rotates counter-clockwise around the $\alpha\beta$ coordinate system when the electrical speed ω_e is positive and the electrical rotor angle θ_e is defined as the angle between the α-axis and the d-axis, the transformation equations between these two coordinate systems are

$$\begin{bmatrix} x_d \\ x_q \end{bmatrix} = \begin{bmatrix} cos(\theta_e) & sin(\theta_e) \\ -sin(\theta_e) & cos(\theta_e) \end{bmatrix} \begin{bmatrix} x_\alpha \\ x_\beta \end{bmatrix} \tag{2.3}$$

$$\begin{bmatrix} x_\alpha \\ x_\beta \end{bmatrix} = \begin{bmatrix} cos(\theta_e) & -sin(\theta_e) \\ sin(\theta_e) & cos(\theta_e) \end{bmatrix} \begin{bmatrix} x_d \\ x_q \end{bmatrix} \tag{2.4}$$

2.1.1.3 Transformation between the abc and dq coordinate systems (Park transformation)

The transformation between the abc and dq coordinate systems can be derived by combining equations 2.1, 2.2, 2.3, 2.4, giving:

$$\begin{bmatrix} x_d \\ x_q \end{bmatrix} = C_{3s/2s} \begin{bmatrix} cos(\theta_e) & cos(\theta_e - 120\,\mathrm{deg}) & cos(\theta_e + 120\,\mathrm{deg}) \\ -sin(\theta_e) & -sin(\theta_e - 120\,\mathrm{deg}) & -sin(\theta_e + 120\,\mathrm{deg}) \end{bmatrix} \begin{bmatrix} x_\alpha \\ x_\beta \end{bmatrix} \tag{2.5}$$

$$\begin{bmatrix} x_a \\ x_b \\ x_c \end{bmatrix} = C_{2s/3s} \begin{bmatrix} cos(\theta_e) & -sin(\theta_e) \\ cos(\theta_e - 120\,\mathrm{deg}) & -sin(\theta_e - 120\,\mathrm{deg}) \\ cos(\theta_e + 120\,\mathrm{deg}) & -sin(\theta_e + 120\,\mathrm{deg}) \end{bmatrix} \begin{bmatrix} x_d \\ x_q \end{bmatrix} \tag{2.6}$$

For the power invariant transformation, $C_{3s/2s} = \sqrt{\frac{2}{3}}$, $C_{2s/3s} = \sqrt{\frac{2}{3}}$. For the amplitude invariant transformation, $C_{3s/2s} = \frac{2}{3}$ and $C_{2s/3s} = 1$. The amplitude invariant form is used throughout this project report.

2.1.2 Modelling of the Synchronous Reluctance Machine

In this section, the modelling of the SynRM is carried out in the dq coordinate system, because the control scheme used in this project report is analysed based on the dq coordinate system. A SynRM without saturation is considered. Figure 2.3 shows the equivalent circuits of a SynRM in a synchronous rotating (dq) frame.

2.1.2.1 Electrical Equations

The general voltage input equation of the SynRM in the dq coordinates can be expressed as:

$$\begin{aligned} v_d &= R_s i_d + \frac{d\psi_d}{dt} - \omega_e \psi_q \\ v_q &= R_s i_q + \frac{d\psi_q}{dt} + \omega_e \psi_d \end{aligned} \tag{2.7}$$

For the standard way of modeling the SynRM with decoupled parameters, constant apparent inductances are introduced. This helps to formulate the flux linkage ψ_d, ψ_q by the following equations:

$$\begin{aligned} \psi_d &= L_d i_d \\ \psi_q &= L_q i_q \\ \frac{d\psi_d}{dt} &= L_d \frac{di_d}{dt} \\ \frac{d\psi_q}{dt} &= L_q \frac{di_q}{dt} \end{aligned} \tag{2.8}$$

By using (2.8) in (2.7), the standard model of the SynRM can be derived:

$$\begin{aligned} v_d &= R_s i_d + L_d \frac{di_d}{dt} - \omega_e L_q i_q \\ v_q &= R_s i_q + L_q \frac{di_q}{dt} + \omega_e L_d i_d \end{aligned} \tag{2.9}$$

where $v_d, v_q, i_d, i_q, L_d, L_q, \omega_e$ represent dq axis voltages, currents, inductances and electric rotor speed respectively. This report focuses on modelling the SynRM

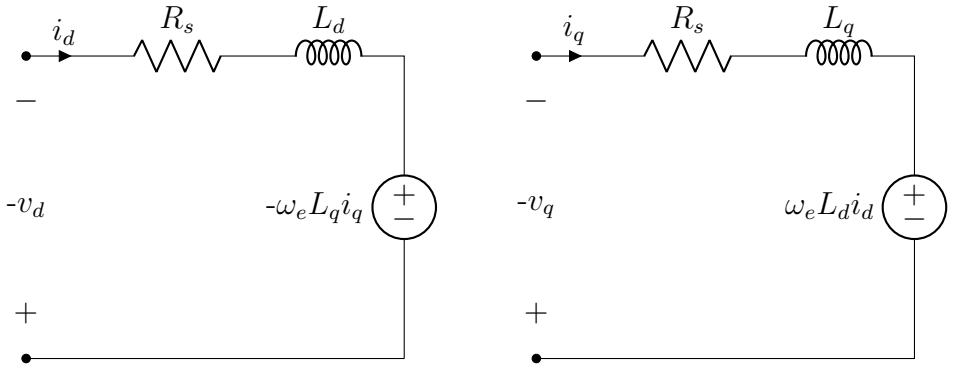

Figure 2.3: Equivalent Circuit of Synchronous Reluctance Machine in a synchronous rotating frame

based on the currents in the dq coordinate frame, thus the variation of temperature, and saturation losses are not included in the analysis. A more accurate electrical state space of the SynRM can be derived by manipulating equation2.9.

$$\begin{aligned} \frac{di_d}{dt} &= -\frac{R_s}{L_d} i_d + \frac{\omega_e L_q}{L_d} i_q + \frac{v_d}{L_d} \\ \frac{di_q}{dt} &= -\frac{R_s}{L_q} i_q - \frac{\omega_e L_d}{L_q} i_d + \frac{v_q}{L_q} \end{aligned} \tag{2.10}$$

2.1.2.2 Mechanical Equations

The electromagnetic torque, mechanical angle and electrical angle can be written as:

$$\begin{aligned} T_e &= \frac{3P}{2}[L_d - L_q] i_d i_q \\ \omega_e &= P\omega_m \\ \theta_e &= P\theta_m \end{aligned} \tag{2.11}$$

The mechanical state space of the SynRM can be expressed as:

$$\begin{aligned} \frac{d\omega_m}{dt} &= \frac{1}{J}[T_e - T_L - B\omega_m] \\ \frac{d\theta_m}{dt} &= \omega_m \end{aligned} \tag{2.12}$$

where $T_e, T_L, \omega_m, \theta_m, \omega_e, \theta_e, P$ represent electromagnetic torque, mechanical load torque, rotor mechanical speed, rotor mechanical angle, rotor electrical speed, rotor electrical angle, pole pairs of the machine, J and B are the inertia of the rotor and viscous friction coefficients, respectively.

2.2 Control Strategies of the SynRM under various operating conditions

Classically, Brushless Direct Current (DC) motors are controlled using a vector control strategy through the application of current or voltage vectors. Under vector control, the current or voltage vector is controlled in both the phase and magnitude. Vector Control of electric motors is generally accepted as a method for extracting good static and dynamic performance of the machine. A brief description of existing control schemes [3] used in industry is given below:

2.2.1 Constant Current in the Inductive Axis Control

This method keeps the current in the most inductive (d- axis) axis constant and varies the current in the least inductive (q-axis) axis to control the torque in the constant torque region. This type of vector control is suitable for applications requiring speed control less than the base value. The torque equation becomes:

$$T_e = \frac{3P}{2}[L_d - L_q] i_d^{constant} i_q^* \tag{2.13}$$

The torque producing current i_q^* is typically controlled using a proportional-integral controller of the speed loop error.

$$i_q^* = K_p(\omega_e^{ref}(t) - \omega_e(t)) + K_i \int_0^t (\omega_e^{ref}(\tau) - \omega_e(\tau))\, d\tau \tag{2.14}$$

where, K_p, K_i, $\omega_e^{ref}(t)$, $\omega_e(t)$ represent the proportional gain of the PI controller, integral gain of the controller, the reference speed in rad/s and current speed in rad/s respectively.

2.2.2 Maximum Torque per Ampere (MTPA) control Strategy

This is the optimum strategy to control the speed of the SynRM from low speed to base speed of the machine while giving maximum drive efficiency. For this strategy, it is necessary to develop a torque expression as a function of the stator currents I_s. It is essentially an approach to maximize the motor torque towards the current, as follows:

$$\begin{aligned} \frac{\delta T_e}{\delta i_d} &= 0 \\ i_s &= \sqrt{i_d^2 + i_q^2} \\ i_d &= i_s cos(\theta_e) \\ i_q &= i_s sin(\theta_e) \\ T_e &= \frac{3P}{4}[L_d - L_q] i_s^2 \frac{sin(2\theta)}{2} \end{aligned} \tag{2.15}$$

The MTPA control strategy has a limited operating region, when the current reaches its boundary I_{max}, the SynRM can generate the maximum electromagnetic torque. The MTPA control strategy has a limited operating region due to the maximum stator current I_{max} allowed.

$$\sqrt{i_d^2 + i_q^2} \leqslant I_{max} \tag{2.16}$$

In the MTPA trajectory, for each stator current, I_s, there is an angle θ_e that maximizes the torque T_e.

2.2.3 Field Weakening Control Strategy

The field weakening control strategy allows the SynRM to operate at above base speed. The Maximum Torque per Volt is an example of the Field Weakening Control method. A maximum torque per volt (MTPV) control strategy is introduced

to improve the high-speed control performance [3]. For the MTPV control strategy, at a given torque value, the optimal point (I_{dq}) which produces the minimum voltage amplitude $\sqrt{v_d^2 + v_q^2}$ should be derived so that the value of 'torque per volt' is maximized.
The MTPV control strategy can be used to achieve very high-speed SynRM control, this can be satisfied if an inverter with a sufficiently high current rating is equipped and the SynRM is able to handle this current overload. Above the base speed, it is necessary to keep the voltage amplitude below the maximum input voltage U_{max}, which is set by the dc-link of the inverter.

$$\begin{aligned} v_d &\approx -\omega_e \psi_q \\ v_q &\approx -\omega_e \psi_d \\ \sqrt{v_d^2 + v_q^2} &= \omega_e \sqrt{\psi_d^2 + \psi_q^2} \leqslant U_{max} \end{aligned} \tag{2.17}$$

To handle the situation when the induced voltage exceeds the voltage limit of the inverter, which would cause the generated torque to decrease, a Field Weakening strategy needs to be applied in order to perform above the base speed of the machine.

Traditionally, these control strategies briefly described in the above sections are applied using a Field Oriented Control (FOC) algorithm, in which cascaded Proportional-Integral (PI) speed and current controllers are utilized to regulate the reference speed as defined by its application. FOC provides good dynamic performance for the machine, however, due to the faster dynamics of power electronics and drive systems used in industry nowadays, Model Predictive Control (MPC) [4] is being explored as an alternative efficient strategy to provide better dynamic and steady-state performance. Despite the computational effort needed to implement this control, the development of faster and more efficient micro-controllers allows the use of more complex system models as well as longer prediction horizons.

2.3 Sensored Control Techniques of the SynRM under various operating conditions

In general, vector control for a SynRM needs information of rotor position in order to make the correct commutation switching for aligning the stator currents for maximum torque production. The position information can either be retrieved by a sensor or by using sensorless control algorithms based on back-emf information or signal injection. In this section three commonly used sensored techniques of vector control will be briefly described.

2.3.1 Optical Encoders

Optical encoders are frequently used for high servo drive systems where position and speed are key for high performance in speed or positioning control. The encoder can provide rotor position for the vector control orientation and may be used for feedback for the speed or torque control loop [5]. There are two types of optical encoders, incremental and absolute. The traditional absolute encoder provides absolute position as binary outputs. The absolute encoder is expensive and used in applications where precision is of uttermost importance, such as robotic arms and surveying apparatus.
Incremental encoders use incremental steps for pulse generation that can be translated to speed and position. The incremental encoder can achieve a fewer number of tracks and is often cheaper compared to an absolute encoder. The drawback of the incremental encoder is that the rotor has to start rotating in order to find the index pulse, thereby the position. While the absolute encoder retrieves the position at startup. Even if high precision position measurements can be achieved by incremental encoders, they still suffer from some quantization errors. The resolution, that is the number of slits per revolution which heavily affects the static quantization error of the encoder. [6]

2.3.2 Resolvers

A resolver is widely used in servo motor applications, for Permanent Magnet Synchronous Motors (PMSM) and SynRM. Resolvers are known for being robust and

reliable in harsh environments and high temperatures [7]. The resolver works as a transformer with one rotating coil and two stationary coils. The two stationary coils are 90 deg mechanically separated. The output signals are generated when the two stationary coils become energized from induction of the rotating coil. For a rotating shaft the two signals become sinusoidal, the position of the rotor can be calculated by a feedback loop calculating the trigonometric identity of the two signals and integrating the speed. [7]

2.3.3 Hall Effect Sensors

Hall sensors are one of the most promising low-cost position sensors for sensor-based motor control. In recent years, Brushless DC Motor drives with Hall position sensors have been targeted for extensive research. The most beneficial property of Hall elements is the low cost and small volume. Hall elements do not require mechanical connection and do not wear out as a resolver or an encoder do [8]. However, the installation of Hall elements inside a rotor is sensitive to displacement and complicated in terms of motor design and fault-tolerant control is preferable for reliable position and speed feedback. Usually, 3 hall elements are installed with a 120 deg mechanical angle separation close to the air gap in the stator. The mechanical angle between two signals is known and therefore the speed of the motor may be calculated for purposes of speed control feedback. Hall elements are commonly used in applications where max torque is required at start-up and close to zero speeds such as in traction applications. [8]

2.4 Estimation Strategies of the SynRM under various operating conditions

Sensorless control of a SynRM implies the interesting challenge of eliminating the mechanical sensors mentioned in the previous section. The replacement of conventional mechanical sensors with soft sensors provides an effective solution and is conducive to improving the reliability of position detection, extending the service life of the motor, simplifying the connection line between the inverter and the motor, reducing system costs and improving the reliability of the system. A

brief literature review of existing state of the art technologies used for sensorless control is presented below:

2.4.1 Literature Review

A literature review of the existing state of the art estimation schemes used in the industry revealed two main approaches used to estimate the position and speed of the rotor divided into the low speed and medium-to-high speed range of the machine: Saliency based methods at standstill and low speed, and the Model-Based Methods for the medium-high speed regions. [1]

2.4.1.1 Saliency Based Methods

Saliency-based methods perform well at a standstill and low speeds. With the injection of high-frequency (HF) voltage signals into the stator windings, the rotor position information is extracted through a heterodyning process and a robust position observer by which the speed may be derived. High-frequency injection methods exploit the saliency information of a machine. Injection signals are directly superimposed in the stator windings with the Field Oriented Control Strategy, the impedance increases with the injection frequency, and it results in an increased voltage [9].
The performance of sensorless control depends on the amplitude and frequency of the injection signals, as the larger the amplitude and frequency, the more accurately it predicts the rotor position, therefore a compromise between accurate estimation performance, increased system bandwidth with improved dynamic performance, and increased current and torque ripples in the motor, which can lead to deterioration in motor performance over time, is needed.
The brief steps describing the design of the robust position observer [10] are listed below:

1. The high frequency current induced by the voltage injection signal is extracted through the use of a high pass filter from the current information of the motor.

2. A demodulation process to generate a normalized position error signal designed using the filtered currents.

3. The position observer is designed based on the SynRM mechanical state space model, equation (2.12), which takes the normalized position error as its inputs and outputs the rotor speed and position.

The two main types of Voltage Injection Signals explored in this literature review are Pulsating Sinusoidal and Square-Wave Signals [9].

- Pulsating Sinusoidal Signal Injection: A sinusoidal sinusoidal voltage pulsating signal is injected along the reference frame of the rotor. The voltage is injected in the d axis resulting in smaller current and torque ripples. However, to ensure the sinusoid of the injected voltage [10], the injection frequency is limited, which is not conducive to an improvement in dynamic performance. The injected voltage signal is as follows:

$$\begin{bmatrix} v_{dh} \\ v_{qh} \end{bmatrix} = \begin{bmatrix} V_h sin(\omega_h t) \\ 0 \end{bmatrix} \tag{2.18}$$

  where V_h is the amplitude of the injected voltage signal and ω_h is its frequency in rad/s.

- Square-Wave Signal Injection: The HF square-wave signal injection-based method has attracted attention for a higher injection frequency and better dynamic performance. Similar to the HF pulsating sinusoidal signal injection-based method, it also injects the HF voltage into the estimated rotor reference frame. The difference is that the injected voltage is a square wave, not a sinusoidal one. Unlike Pulsating Sinusoidal Injection, the filtering process due to the limited injection frequency aggravates the dynamic bandwidth of the sensorless control system. As the injection frequency increases, the dynamics of the sensorless control can be enhanced, and the interference between the injected signal and the fundamental components of the current control can be diminished. [9] The injected voltage signal is:

$$\begin{bmatrix} v_{dh} \\ v_{qh} \end{bmatrix} = \begin{bmatrix} V_h(-1)^k \\ 0 \end{bmatrix} \tag{2.19}$$

  where, V_h is the amplitude of the injected voltage signal and k is its sequence.

2.4.1.2 Model Based Methods

The Model-based method is used to achieve position sensorless control of the SynRM drive system when the motor runs at middle or high speed. The model method estimates the rotor position by the back-EMF model of the fundamental frequency of the excitation. Since the rotor saliency and the additional test signal are not needed, the rotor position information can be estimated only by the motor model , equations (2.10 and 2.12). This model-based method is relatively simple to implement, so the method is widely used in the vector control system for a sensorless SynRM drive. However, the capability of obtaining the rotor position deteriorates dramatically in low-speed operation, as the amplitude of the back electromotive force (EMF) signal becomes too weak to be detected precisely. [11]

- Luenberger Observer: SynRM is modelled in state space in its Extended EMF (EEMF) form with the nominal speed of the machine selected as a parameter in the system matrix [12]. It reconstructs the state variables based on the knowledge of inputs and outputs of the system. The input to the observer are the currents and voltages with rotor position and speed included in the state vector estimated in the feedback. The state observer is based on an extended EEMF model of the SynRM in state space where the observer gains are selected using a traditional pole placement method or a pole-placement using Convex Optimization via Linear Matrix Inequalities approach.
  The Luenberger Observer provides an interesting solution as it allows different configurations to satisfy user requirements such as defining the performance objectives (stability, filtering) as a convex optimization problem to be solved by minimizing the H_∞ norm which leads to the H_∞ Observer approach.
  The stability of the Luenberger observer is important in providing accurate position information. Loss of observer stability would cause erratic and destructive motor operation. To keep the controlled system stable, the gain in the observer has to be optimized. Determining the optimum gain of the observer under all operating conditions will lead to practical difficulties and limitations. Moreover, initial states are required for proper convergence of the observer. Due to these shortcomings, the state observer method is not

the most commonly used method at the moment and more research is still being done on this approach.

- Nonlinear Kalman Filters: The Kalman filter is an optimal observer that estimates the unmeasured variables for Linear Time Invariant (LTI) systems with a Gaussian noise, minimizing the error covariance of the state estimate [13]. The estimation is achieved by two steps. First, the actual state is predicted using the dynamic model of the system and the known input. Next, an update step is achieved based on the error between the measurements and the predicted output. The Kalman filter is useful in various applications and is computationally simple to implement. There are two main kinds of the nonlinear Kalman Filter:

  - Extended Kalman Filter (EKF): The Extended Kalman Filter is a Kalman filter applied to a nonlinear system by linearization of the model around the state estimate. The EKF is the most widely used algorithm for state estimation of nonlinear systems; however, it can be difficult to tune and can give wrong state estimates if the system nonlinearities are severe, which causes linearization issues. [1]
  - Unscented Kalman Filter (UKF): Based on the unscented transformation theory, the UKF does a better job than EKF of estimating the nonlinear states of the system by replacing the linearization step of the EKF with unscented transformations for propagating the mean and covariances. [1] [14]

  The non-linear Kalman filter explored in this report is the Extended Kalman Filter.

- Particle Filter: The Particle Filter is a recursive Bayesian state estimator that uses discrete particles to approximate the posterior distribution of the estimated variables. The particle filter has some similarities with the UKF in that it transforms a set of points via known nonlinear equations and combines the results to estimate the mean and covariance of the state. However, in the particle filter the points are chosen randomly, whereas in the UKF the

points are chosen on the basis of a specific algorithm. Because of this, the number of points used in a particle filter generally needs to be much larger than the number of points in a UKF. Another difference between the two filters is that the estimation error in a UKF does not converge to zero in any sense, but the estimation error in a particle filter does converge to zero as the number of particles (and hence the computational effort) approaches infinity. Hence, as it is a computationally heavy algorithm, it is rarely used in industrial applications [15].

2.5 Two-Level Voltage Source Inverter

2.5.1 Switching States of the two-level voltage source inverter

The Two-level Voltage Source Inverter (VSI) has been widely used in different electrical applications for its simple configuration and proven technology. Figure 2.4 shows the topology of a two-level VSI and the relationship between the switching states and the $\alpha\beta$ coordinate system.

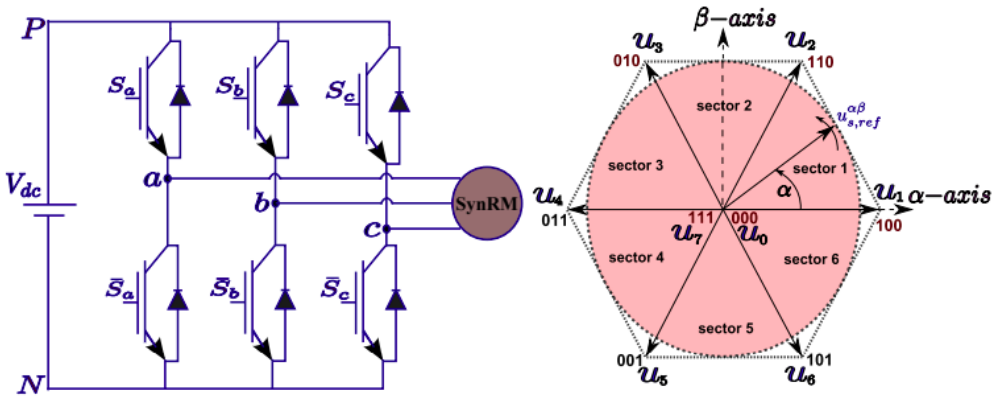

Figure 2.4: Voltage Source Inverter and Relation between switching states and the $\alpha\beta$ coordinate system

2.5.2 States of the Inverter:

In the derivation of operational constraints, it is assumed that a three-phase 2Level - VSI inverter is used in the implementation of the current control. The operation of the three-phase 2Level -VSI inverter and its states is illustrated in Table 2.1. In

Conducting Modes	Switching States			Output vectors	
	Sa	Sb	Sc	V_α	V_β
u_0	0	0	0	0	0
u_1	1	0	0	$\frac{2V_{dc}}{3}$	0
u_2	1	1	0	$\frac{V_{dc}}{3}$	$\frac{\sqrt{3}V_{dc}}{3}$
u_3	0	1	0	$-\frac{V_{dc}}{3}$	$\frac{\sqrt{3}V_{dc}}{3}$
u_4	0	1	1	$\frac{V_{dc}}{3}$	0
u_5	0	0	1	$-\frac{V_{dc}}{3}$	$-\frac{\sqrt{3}V_{dc}}{3}$
u_6	1	0	1	$\frac{V_{dc}}{3}$	$-\frac{\sqrt{3}V_{dc}}{3}$
u_7	1	1	1	0	0

Table 2.1: Conducting Modes and Corresponding $V_{\alpha\beta}$

order to have a convenient regulation for the voltage vectors of the two-level VSI, the switching states need to be transformed into the $\alpha\beta$ coordinates. The phase angle difference between each phase leg is $2\pi/3$, the coordinate transformation method can be derived as:

$$\begin{bmatrix} V_\alpha \\ V_\beta \end{bmatrix} = \frac{2}{3} V_{dc} \begin{bmatrix} 1 & -\frac{1}{2} & -\frac{1}{2} \\ 0 & -\frac{\sqrt{3}}{2} & -\frac{\sqrt{3}}{2} \end{bmatrix} \begin{bmatrix} S_a \\ S_b \\ S_c \end{bmatrix} \tag{2.20}$$

where, V_{dc} is the DC-link voltage of the two level VSI, $S_{a,b,c}$ represents the switching states and the amplitude invariant factor $C_{3s/2s} = \frac{2}{3}$ is used.

2.5.3 Space vector pulse width modulation scheme (SVPWM)

Space Vector Pulse Width Modulation (SVPWM) is a commonly used modulation scheme for the field oriented control of the Brushless DC Motor [16]. The two-level VSI block of the benchmark system (introduced in Chapter 4) generates the required voltage vectors from the PI controller by using the SVPWM scheme.

As can be seen in Figure 2.5, a reference voltage vector U_{ref} can be derived by taking the average in one switching interval T_{sw} as (equation 2.21) shows. $\frac{U_{dc}}{\sqrt{3}}$is the rated output voltage (radius of the inscribed circle) based on the maximum circular SVPWM scheme.

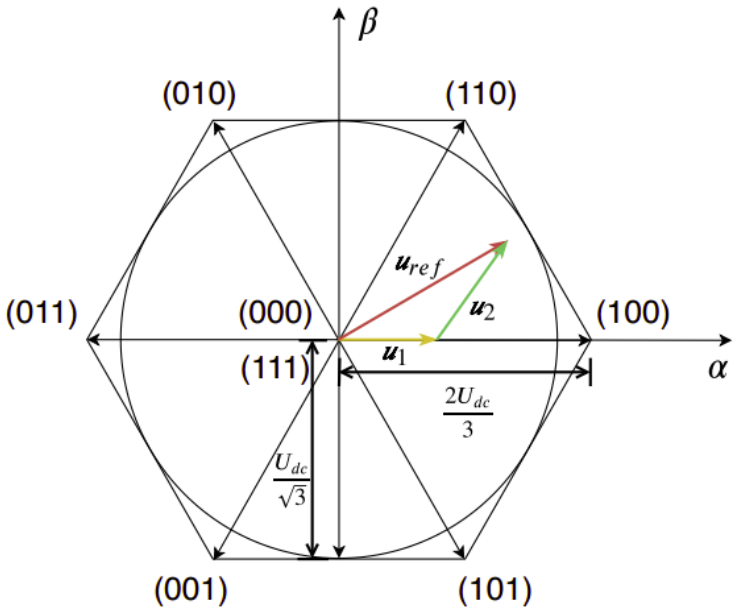

Figure 2.5: Voltage Vectors under SVPWM scheme

$$
\begin{aligned}
T_{(100)} &= |\frac{u_1}{u_{(100)}}|T_{sw} \\
T_{(110)} &= |\frac{u_2}{u_{(120)}}|T_{sw} \\
T_{000} &= T_{sw} - (T_{100} + T_{110}) \\
u_{ref} &= u_{(100)}T_{(100)} + u_{(110)}T_{(110)} + u_{(000)}T_{(000)}
\end{aligned}
\tag{2.21}
$$

Compared to using the eight switching states directly, the SVPWM scheme enables the two-level VSI to generate more selections of the required voltage vector by the method of averaging. In addition, the SVPWM scheme helps to reduce the total harmonic distortion and the current and torque ripples.

Chapter 3

Method

This chapter presents the design of the control and observer strategies for sensorless speed control of the SynRM. The first part of this chapter presents the design of the implemented control system. The second part presents the design of the Extended Kalman Filter for sensorless control in order to observe rotor speed and position, stator currents, and mechanical load torque.
The architecture of the Proposed Sensorless Finite Control Set Direct Speed Predictive Control of the SynRM is displayed in figure 3.1.

3.1 Controller Design

3.1.1 Model Predictive Control

For electric drives, conventional control methods are linear control schemes with the help of a pulse width modulation scheme and nonlinear control schemes in the form of hysteresis bounds. But the drawback of these methods is that they cannot perform well when it comes to the physical constraints and parameter variations, such as limited current amplitude and its slew rate, variations of resistance, the flux at elevated temperature, and so on. To control such constrained systems, the model predictive control (MPC) method has been applied in the area of electric drives and power electronics. In comparison to classical control approaches in the field of electrical drives and power electronics like the FOC, the MPC approach is able to provide higher dynamic performance of the machine [17].
Due to recent technological advances in power electronics, embedded processing

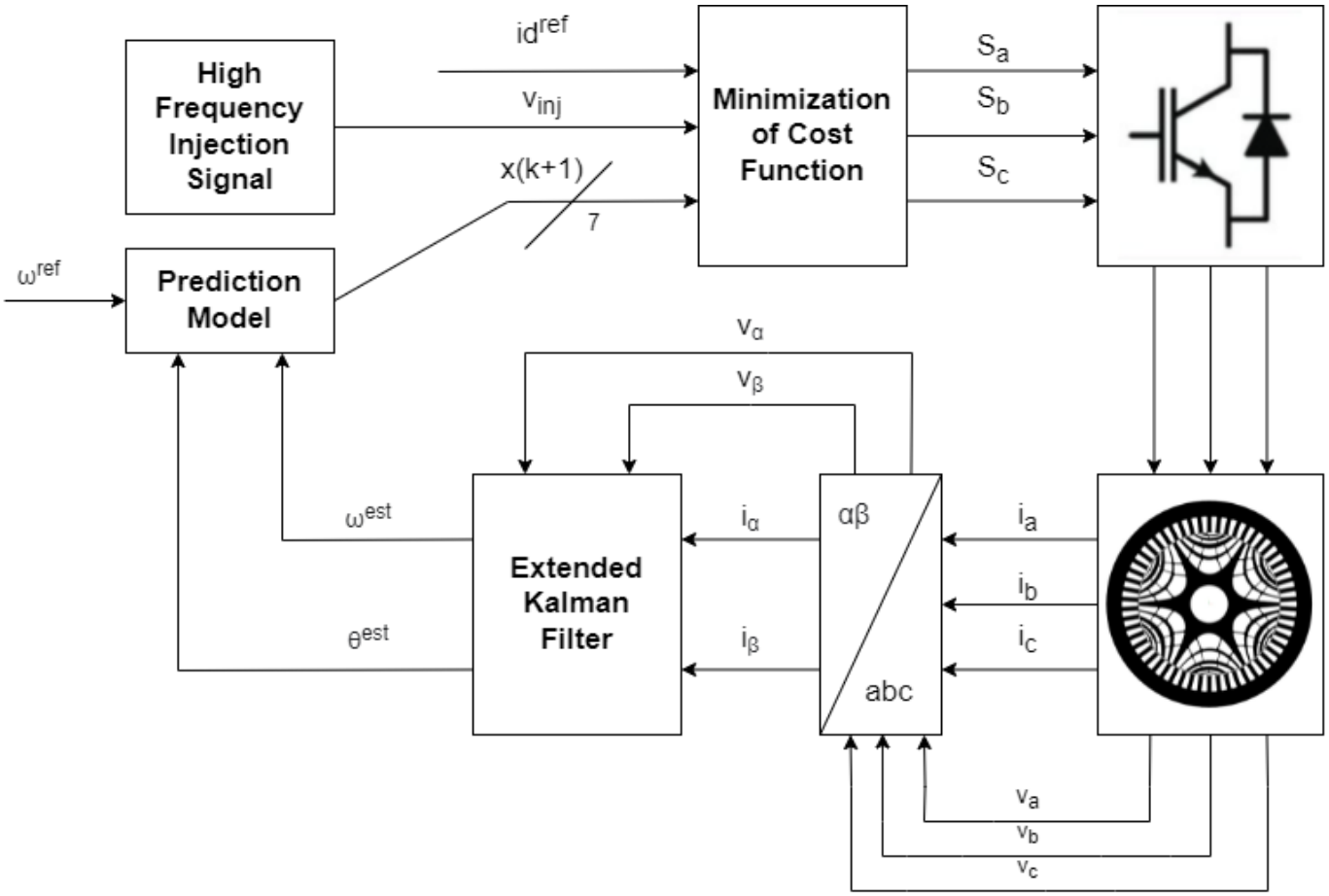

Figure 3.1: Proposed Finite Control Set Direct Speed Predictive Control (DSPC) Architecture

hardware, and signal processing fields, the realization of complex control and estimation strategies can be implemented on digital signal controllers to accomplish different objectives in varying operating regions.

3.1.1.1 Overview of MPC operation

As MPC is a discrete-time control operation, a discrete dynamic model of the electric drives is needed to predict its future states. The number of predicted future time steps is defined as the prediction horizon, N_p. A control objective is formulated as a quadratic optimization problem that minimizes a certain cost function, typically a convex function of predicted system states x and control input u, over a prediction horizon N_p using the control input as an optimization variable while respecting system dynamics and static constraints. This results in an optimal control sequence that steers the system towards the desired trajectory.
The main advantage of MPC is that it can handle constraints systematically and solving constrained finite horizon optimal control problems in a receding horizon fashion by fixing the origin of the time axis at the current step and then predicting the future evolution of system states over a short horizon. (see Figure 3.2)

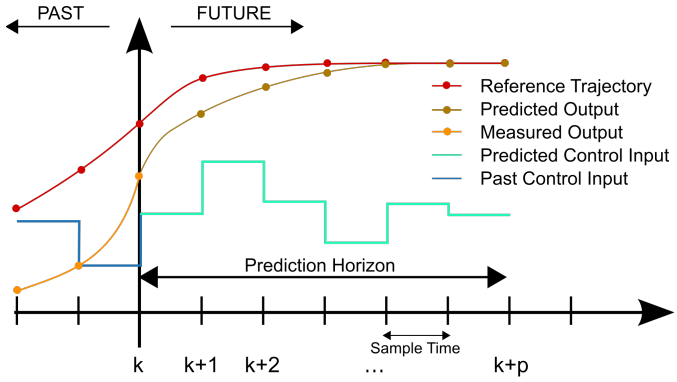

Figure 3.2: The receding horizon scheme of model predictive control

3.1.1.2 MPC for electric drives

The predictive control of electric drives, in general, is based on finite horizon optimization of the current I_{dq} states of the machine. At each sampling time, starting

at the current state, an open-loop optimal control problem is solved over a finite horizon. The computed optimal manipulated signal is applied to the system only during the following sampling interval. At the next time step, a new optimal control problem based on new measurements of the states is solved over a shifted horizon. Furthermore, the optimization of the inverter states is performed using the receding horizon control principle, which is the core of model predictive control [17].

Depending on how the input voltage vectors are formulated for states prediction, MPC for electric drives can be classified into two different types, Continuous Control Set MPC (CCS-MPC) [18] and Finite Control Set MPC (FCS-MPC) [2]. For CCS-MPC, a continuous set of the voltage vectors is evaluated in the cost function, the optimal voltage vector can be generated with the help of an SVPWM scheme inverter. The FCS-MPC directly optimizes the inverter states with the optimal voltage vector hence, the SVPWM is not required in its implementation, which simplifies the development. Since for a two-level Voltage Source Inverter (VSI), there are eight combinations of inverter states, the terminology of a finite control set (FCS) is defined. [19]

The FCS-MPC is the control scheme used in this report.

3.1.2 Discretization of the SynRM Model

In order to realize the FCS-MPC current control algorithm for the SynRM, a discretized SynRM model is needed to predict the states of the SynRM over a certain prediction horizon, N_p ($\geqslant 1$).

There are several popular methods for implementing the discretization of a state-space model: The Forward Euler method, the Tustin method, and the Zero-order Hold method. The discretization method used in this report is the Forward Euler Method. The derivation of the discretization starts from the continuous-time electrical model of the SynRM derived in equation 2.10, of which a generalized parameter varying state-space symbolic equation can be written as:

$$\dot{x}(t) = A(\omega_e)x(t) + Bu(t) \tag{3.1}$$

$$\begin{bmatrix} \frac{di_d}{dt} \\ \frac{di_q}{dt} \end{bmatrix} = \begin{bmatrix} \frac{-R_s}{L_d} & \frac{\omega_e L_q}{L_d} \\ \frac{-\omega_e L_d}{L_q} & \frac{-R_s}{L_q} \end{bmatrix} \begin{bmatrix} i_d \\ i_q \end{bmatrix} + \begin{bmatrix} \frac{v_d}{L_d} \\ \frac{v_q}{L_q} \end{bmatrix} \tag{3.2}$$

where,

$$\begin{aligned} x = \begin{bmatrix} i_d \\ i_q \end{bmatrix}, u = \begin{bmatrix} v_d \\ v_q \end{bmatrix} \\ A = \begin{bmatrix} \frac{-R_s}{L_d} & \frac{\omega_e L_q}{L_d} \\ \frac{-\omega_e L_d}{L_q} & \frac{-R_s}{L_q} \end{bmatrix}, B = \begin{bmatrix} \frac{1}{L_d} & 0 \\ 0 & \frac{1}{L_q} \end{bmatrix} \end{aligned} \tag{3.3}$$

The system matrix A $\in$: $\mathbb{R}^x$, input matrix B $\in$: $\mathbb{R}^u$ of the state space model are derived based on the system and input matrices of the continuous-time state-space model.

3.1.2.1 Forward Euler Method

For the Forward Euler method, $u(t), x(t)$ and $\dot{x}(t)$ can be transformed to $u(k), x(k)$ and $\frac{x(k+1)-x(k)}{T_s}$ respectively in discretized form. The derivation process is shown below.

$$\begin{aligned} \frac{x(k+1) - x(k)}{T_s} &= Ax(k) + Bu(k) \\ x(k+1) &= T_s(Ax(k) + Bu(k)) + x(k) \\ x(k+1) &= (AT_s + I)x(k) + BT_s u(k) \\ x(k+1) &= A_d x(k) + B_d u(k) \end{aligned} \tag{3.4}$$

where, I is the identity matrix of the same size as A. The electrical and mechanical discretized state-space model becomes:

$$\begin{aligned} i_d[k+1] &= (1 - T_s \frac{R_s}{L_d}) i_d + T_s \frac{L_q}{L_d} \omega_e[k] i_q[k] + T_s \frac{v_d[k]}{L_d} \\ i_q[k+1] &= (1 - T_s \frac{R_s}{L_q}) i_q + T_s \frac{L_d}{L_q} \omega_e[k] i_d[k] + T_s \frac{v_q[k]}{L_q} \end{aligned} \tag{3.5}$$

Following the steps above, the mechanical discretized state space model using equation 2.12 becomes:

$$\begin{aligned} \omega_m[k+1] &= \omega_m[k] + \frac{T_s}{J}(T_e[k] - T_L - B\omega_m[k]) \\ \omega_e[k+1] &= P\omega_m[k+1] \\ \theta_m[k+1] &= \omega_m[k] + T_s(\omega_m[k]) \\ \theta_e[k+1] &= P\theta_m[k+1] \end{aligned} \tag{3.6}$$

3.1.3 Execution of the FCS-MPC Control Algorithm :

In this report, the FCS-MPC scheme is utilized to realize the SynRM speed control operation.Figure 3.3 graphically shows the FCS-MPC execution process, and details are explained in the following subsections.

3.1.3.1 Measurements

The FCS-MPC algorithm starts by taking the controller reference values, the current reference on the d axis, $i_d^{ref}[k]$ and the speed reference in rpm, $\omega_m^{ref}[k]$, estimated signals from the observer (EKF) of the dq currents, $i_d^{est}[k]$, $i_q^{est}[k]$, electrical rotor speed $\omega_e^{est}[k]$, electrical angle $\theta_e^{est}[k]$ and the load torque $T_L^{est}[k]$ in the current time step k.

3.1.3.2 Prediction

1. Voltage vector pre-selection:
   As mentioned briefly in chapter 2, eight switching states in total can be generated by a two-level VSI. All inverter phase legs change the switching state instantaneously in its ideal form hence, all eight switching states can be reachable in one-time step. Table 2.1 presents all the possible selections of each switching state. Then the pre-selected stator voltage vectors v_{dq} are represented as a function of the switching vectors S_{abc} of the 3-phase two

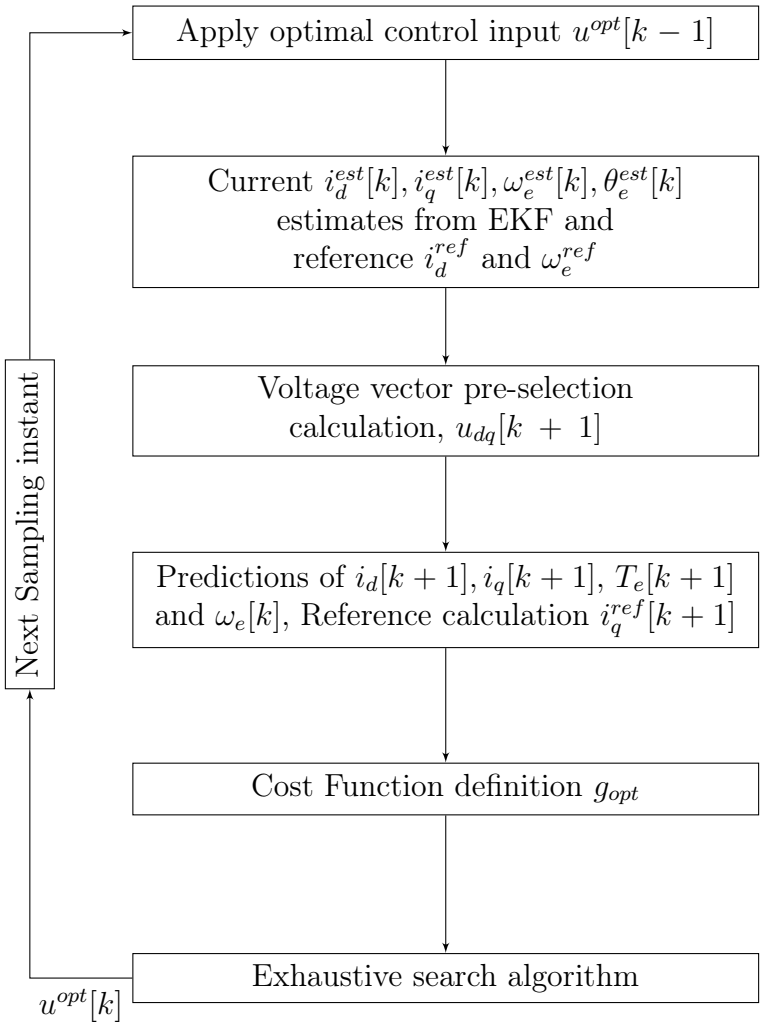

Figure 3.3: Execution process of FCS-MPC

level voltage source inverter:

$$\begin{aligned} v_{dq}[k+1] &= T_p(\hat{\theta}_e(k))^{-1} \cdot T_c \cdot V_{dc} \cdot S_{abc}[k+1] \\ S_{abc}[k] &= \frac{2}{3}(S_a[k] + aS_b[k] + a^2 S_c[k]) \\ T_p(\hat{\theta}_e)^{-1} &= \begin{bmatrix} cos(\theta_e) & sin(\theta_e) \\ -sin(\theta_e) & cos(\theta_e) \end{bmatrix} \\ T_c &= \begin{bmatrix} 1 & -\frac{1}{2} & -\frac{1}{2} \\ 0 & \frac{\sqrt{3}}{2} & -\frac{\sqrt{3}}{2} \end{bmatrix} \end{aligned} \tag{3.7}$$

where, T_c and $T_p(\hat{\theta}_e)^{-1}$ represents the Clarke and inverse Park transformation, V_{dc} represents the DC-link voltage of the inverter, $a = e^{j\frac{2\pi}{3}}$ and S_a, S_b, S_c represent the switching states of the inverter from table 2.1. These eight vectors can be applied to predict the future values of the current, with the first and final candidate sets (u_0 and u_7) being the zero vectors. Hence, only the first seven vectors ($u_0 - u_6$) are evaluated.

2. Angle Compensation:
   In equation 3.6, when transferring the voltage vectors into the dq coordinate system, a constant electrical angle $\theta_e(k)$ at time step k is used. To improve the accuracy of selecting the voltage vectors, the angle compensation method which takes the angle variations into consideration can be utilized for help [20]. Instead of the electrical angle $\theta_e(k)$, it is assumed that the electrical rotating speed $\omega_e(k)$ is constant during each time interval. Thus the electrical angle $\theta_e(k)$ varies as:

$$\theta_e(t) = \omega_e(t_k)(t - t_k) + \theta_e(t_k), \quad t_k \leqslant t < t_k + T_s \tag{3.8}$$

   Therefore, the voltage vectors in the $\alpha\beta$ coordinate system rotate with a constant speed $\omega_e(k)$ during the time interval t_k to $t_k + T_s$. The mean value of the electrical angle θ_e of the varying voltage vectors will be derived, and the pre-selection of input voltage vectors at time step $k+1$ can be approximated as:

$$\begin{aligned} \theta_e(k+1) &\approx \omega_e(k) + \frac{T_s}{2}\omega_e(k) \\ v_{dq}[k+1] &= T_p(\hat{\theta}_e(k+1))^{-1} \cdot T_c \cdot V_{dc} \cdot S_{abc}[k+1] \end{aligned} \tag{3.9}$$

3. States Prediction:
   With the help of the discretized model of the SynRM equations 3.4 and 3.5, future state future values of i_d and i_q can be predicted by applying the set of pre-selected voltage vectors as input.
   At time step k, the state prediction equations can be defined as:

$$\begin{aligned} x(k+1) &= A_d(k)x(k) + B_d(k)u(k-1) \\ x(k+2) &= A_d(k+1)x(k+1) + B_d(k+1)u(k) \end{aligned} \tag{3.10}$$

   The explanation of how the prediction of the states works is listed below.

   (a) For the first equation, to predict the states $x(k+1)$ at the next time step $k+1$, the voltage vector $u(k-1)$ is selected at the previous step $k-1$ and is applied as the input to the system.

   (b) With a prediction horizon $N_p = 1$, for the second equation, $u(k)$ has 7 possible values to generate the SynRM at the next time step $k+1$. By applying these 7 values to the second equation, 7 corresponding states $x(k+2)$ can be derived. A verification of how these seven states operate is made based on the cost functions (in the next section) and the corresponding control decision vector that minimizes the cost function is chosen as optimal. This optimal voltage vector will be selected as an input at the next time step $k+1$.

   (c) More prediction equations are needed if a higher prediction horizon is chosen. This implementation is similar to that described in the previous steps.

3.1.3.3 Cost Function

An objective function is required to reflect the purpose of the predictive speed controller. The computation of the cost function is minimized using the absolute L_1 norm as it is computationally cheaper than the L_2 norm and the optimal control inputs for the system need to be executed in milliseconds [2]. The controller objectives are focused on:

- Speed reference tracking

- Smooth behavior of the electrical torque
- Torque per ampere optimization
- Current magnitude limitation for over current protection

Subsequently, exploiting these objectives, the cost function for speed control with one sampling prediction horizon can be stated as follows.

$$g_s = \lambda_\omega(\omega_m[k+1] - \omega_m^{ref}[k+1])^2 + \lambda_{T_e}(T_e[k] - T_L[k])^2 \tag{3.11}$$

where λ_ω and λ_{T_e} are weighting factors for speed and torque. Minimizing the cost function can be achieved by setting the first derivative of the cost function equal to zero. Using equations 3.6 and 3.11 and assuming that the load torque T_L is constant, the derivative result can be defined as

$$\frac{\partial g_s}{\partial T_e} = \frac{2\lambda_\omega T_s}{J}(\omega_m[k+1] - \omega_m^{ref}[k+1]) + 2\lambda_{T_e}(T_e[k]) = 0 \tag{3.12}$$

So, the reference electromagnetic torque can be calculated from equation 3.12 as follows:

$$T_e[k] = \frac{\lambda_\omega T_s}{\lambda_e J}(\omega_m^{ref}[k+1] - \omega_m[k+1]) \tag{3.13}$$

If the reference direct current i_d^{ref} is kept constant, then the reference quadrature current i_q^{ref} at the time step (k + 1) can be calculated from equations 3.5, 3.6 and 3.13 as:

$$i_q^{ref} = \frac{T_e[k]}{\frac{3}{2}P(L_d - L_q)i_d^{ref}} \tag{3.14}$$

Finally, using equations 3.11 and 3.14, the proposed cost function with current magnitude limitation becomes:

$$\begin{aligned} g_{opt} = (i_d^{ref}[k+1] - i_d[k+1])^2 + (i_q^{ref}[k+1] - i_q[k+1])^2 + \\ \begin{cases} 0 & if \quad \sqrt{i_d[k+1]^2 + i_q[k+1]^2} \quad \leq i_{s,max} \\ \infty & if \quad \sqrt{i_d[k+1]^2 + i_q[k+1]^2} \quad \geq i_{s,max} \end{cases} \end{aligned} \tag{3.15}$$

where, $i_{s,max}$ is the maximum stator currents of the SynRM. To execute the Speed Predictive Control algorithm, the estimation of the position, speed and load torque T_L is required. Hence, an extended Kalman Filter is used to observe these signals.

3.2 Observer Design - Proposed Extended Kalman Filter with High Frequency Injection for Whole Speed range of the SynRM

A nonlinear observability analysis of the SynRM has been performed extensively in [21], and revealed using a local weak observability analysis that, in steady state, when the current derivatives are zero, the SynRM is observable at any speed different from zero. To guarantee observability at zero speed, the derivatives of the currents must be nonzero, highlighting the need for some kind of high-frequency current injection.

Based on this realization, a single nonlinear Kalman filter using HF injection and back emf information is proposed. At low speed, a HF voltage signal is injected to produce the desired variations in the stator currents required for the system to be locally weakly observable, and at medium-high speed, it uses the fundamental information from the back emf of the machine.

3.2.1 Extended Kalman Filter (EKF) Formulation:

To design the EKF, a nonlinear state-space model of the SynRM in the synchronous reference frame $d-q$ is required. The available measurements are typically only the stator currents, which are measured directly in the stationary($\alpha\beta$) frame regardless of the coordinates in which the machine is being modeled. The current and voltage signals fed into the EKF are in the stationary frame $\alpha\beta$. The nonlinear state-space model of SynRM can be expressed as

$$\begin{aligned} \dot{x} &= g(x,u) \\ y &= h(x) \end{aligned} \tag{3.16}$$

where x, y and u are the state, output and input vectors, respectively, and are described as:

$$\begin{aligned} x &= [i_d, i_q, \omega_e, \theta_e, T_L]^T \\ y &= [i_\alpha, i_\beta]^T \\ u &= [v_\alpha, v_\beta]^T \end{aligned} \tag{3.17}$$

g(x, u), h(x) can be deduced from equations 2.10, 2.11 and 2.12, as follows:

$$g(x,u) = \begin{bmatrix} -\frac{R_s}{L_d} i_d + \frac{L_q}{L_d}\omega_e i_q + \frac{cos(\theta_e)}{L_d} u_\alpha + \frac{sin(\theta_e)}{L_d} u_\beta \\ -\frac{R_s}{L_q} i_q - \frac{L_d}{L_q}\omega_e i_d - \frac{sin(\theta_e)}{L_q} u_\alpha + \frac{cos(\theta_e)}{L_q} u_\beta \\ \frac{3P^2}{2}[L_d - L_q] i_d i_q - \frac{PT_L}{J} \\ \omega_e \\ 0 \end{bmatrix} \tag{3.18}$$

$$h(x) = \begin{bmatrix} i_\alpha \\ i_\beta \end{bmatrix} = \begin{bmatrix} i_d cos(\theta_e) - i_q sin(\theta_e) \\ i_d sin(\theta_e) + i_q cos(\theta_e) \end{bmatrix} \tag{3.19}$$

The EKF uses a discrete-time nonlinear model of the SynRM from equations 3.5 and 3.6 with system and measurement uncertainties added to it:

$$\begin{aligned} x[k+1] &= x[k] + T_s g(x[k], u[k]) + w[k] \\ y[k] &= h(x[k]) + v[k] \end{aligned} \tag{3.20}$$

where, $w[k]$ is the represented system uncertainties with covariance matrix $Q = E[w[k]w[k]^T)]$, and $v[k]$ is the measurement noise with covariance matrix $R = E[v[k]v[k]^T]$ which are represented as diagonal matrices of appropriate dimensions.The parameters of the covariance matrices have an excessive influence on the response and EKF convergence. They are manually iteratively tuned, which takes a lot of time and effort, but a better idea is to tune them using a stochastic optimization algorithm, such as particle swarm optimization or ant colony optimization [22]. The EKF can be broken down into Prediction and Correction steps which are summarized in algorithm 1 below:

Algorithm 1 EXTENDED KALMAN FILTER

Initialization for k = 0:

x_0, Q, R are set with initial values using Particle Swarm Optimization

Prediction Step:

(a) State Prediction at sampling time [k+1]

$x[k+1] = x[k] + T_s g(x[k], u[k]) = f(\hat{x}[k], u[k])$

(b) Prediction of error covariance matrix.

$P[k+1] = A[k+1]\hat{P}[k]A^T[k+1] + Q$

where, A is the Jacobian matrix of the state matrix f(x,u)

$A[k+1] = \frac{\partial}{\partial x}[f(x,u)]_{\hat{x}[k]}$

Computation of the Kalman Gain:

$K[k+1] = P[k+1]h^T[k+1][h[k+1]P[k]h^T[k+1] + R]^{-1}$

Correction Step:

(a) States Updating $\hat{x}[k+1] = x[k+1] + K[k+1][y[k+1] - \hat{y}[k+1]]$

(b) Updating error covariance P

$\hat{P}[k+1] = P[k+1] - K[k+1]h[k+1]P[k+1]$

Update Step

Put $k = k+1, x[k] = x[k+1], P[k] = P[k+1]$, and return to to the prediction step.

where, the Jacobian matrix A is:

$$A = \begin{bmatrix} -\frac{R_s}{L_d} & \frac{L_q}{L_d}\omega_e & \frac{L_q}{L_d}i_e & -\frac{sin(\theta_e)}{L_d}u_\alpha + \frac{cos(\theta_e)}{L_d}u_\beta & 0 \\ -\frac{L_d}{L_q}\omega_e & -\frac{R_s}{L_q} & -\frac{L_d}{L_q}i_d & -\frac{cos(\theta_e)}{L_d}u_\alpha - \frac{sin(\theta_e)}{L_d}u_\beta & 0 \\ \frac{3P^2}{2}[L_d - L_q]i_q & \frac{3P^2}{2}[L_d - L_q]i_d & 0 & 0 & -\frac{P}{J} \\ 0 & 0 & 1 & 0 & 0 \\ 0 & 0 & 0 & 0 & 0 \end{bmatrix} \tag{3.21}$$

3.2.2 High Frequency (HF) Injection Transition Strategy:

A simple transition strategy is applied, with the HF injection turned off or on based on the speed estimate being less than 10% of the rated speed of the machine. It is a simple relational operation that does not affect the smoothness of the operation.

Algorithm 2 High Frequency Injection (HFI) Transition Strategy

Initialization:
If rated speed $\leq$ 10 % of rated speed (rpm)
then:
activate HFI
else:
return 0

3.2.3 Improvement of Controller Cost Function to minimize High Frequency (HF) Content

Due to lack of the pulse width modulation (PWM) module, it is difficult to implement conventional high frequency signal injection sensorless control method on finite-control-set model predictive control (FCS-MPC). Hence a simple method using a voltage reference tracking is added as a controller objective.
In order to minimize the high frequency content generated in the low speed range by the observer, an additional term corresponding to HF voltage reference is added to the controller cost function. This becomes:

$$\begin{aligned} g_{opt} = (i_d^{ref}[k+1] - i_d[k+1])^2 + (i_q^{ref}[k+1] - i_q[k+1])^2 \\ +\lambda_{hf}(v_d[k+1] - (v_d^{ref}[k+1] + v_{inj}[k+1]))^2 \\ \begin{cases} 0 & if \quad \sqrt{i_d[k]^2 + i_q[k]^2} \quad \leq i_{s,max} \\ \infty & if \quad \sqrt{i_d[k]^2 + i_q[k]^2} \quad \geq i_{s,max} \end{cases} \end{aligned} \tag{3.22}$$

$$v_d^{ref}[k] = R_s i_d^{est}[k] + L_d \frac{i_d^{ref}[k] - i_d^{est}[k]}{T_s} - \omega_e^{est}[k] L_q i_q^{est}[k] \tag{3.23}$$

where, v_{inj} is the demand value of the injected voltage component, v_d is the predicted stator voltage in the d-axis, v_d^{ref} is the reference voltage in the d-axis and λ_{hf} is the weight of the additional term for high frequency minimization.

3.2.4 Tuning of Controller Weighting Factors and EKF Covariance Matrices

It has been proposed in [22], that swarm intelligence methods like the Particle Swarm Optimization (PSO) or Ant Colony Optimization can be used to tune the

measurement and process noise covariance matrices of the Kalman Filters. In [23], PSO is used to tune the proportional and integral gains of a control system for an robotic system. In this report, the PSO is used to tune the filter. In this system, the cost function which is used to select the best parameters is represented as follows:

$$\begin{aligned} min(\omega^{cost}) &= \sum(\omega_{ref} - \omega_{est}) \\ min(\omega_{est}^{cost}) &= \sum(\omega_{r} - \omega_{est}) \\ min(I_{d}^{cost}) &= \sum(I_{d}^{ref} - I_{d}^{est}) \end{aligned} \tag{3.24}$$

Chapter 4

Simulation Study, Results & Analysis

4.1 Simulation Setup

A drive system that includes cascaded PI speed and current controllers, SVPWM that implements the FOC-based control scheme, and a SynRM model is used as a benchmark for the MPC controller designed in the report. A simulation bench is developed in Simulink, to include a drive system with a virtual dynamometer (dyno for short). (see Figure 4.1)
For the benchmark system (see figure 4.2):

- The estimated ω_e is compared to ω_{ref} to obtain the error that is used as input to the proportional-integral (PI) speed controller to produce the reference current on the q-axis, i_q^{ref}
- Using a constant reference d-axis current i_d^{ref} and the reference q-axis current i_q^{ref} calculated from the speed controller, cascaded PI current controllers are used to generate the required voltage that should be applied to the machine.
- The FOC scheme consists of a speed controller, current controllers with constant d-axis reference current and its sampling frequency is 10 kHz. The inverter model can generate the three phase voltages by using the SVPWM scheme to derive the averaged voltage vector during each sampling interval. The inverter switching frequency, using the SVPWM scheme, is 10 kHz, which is synchronized with the FOC controllers.

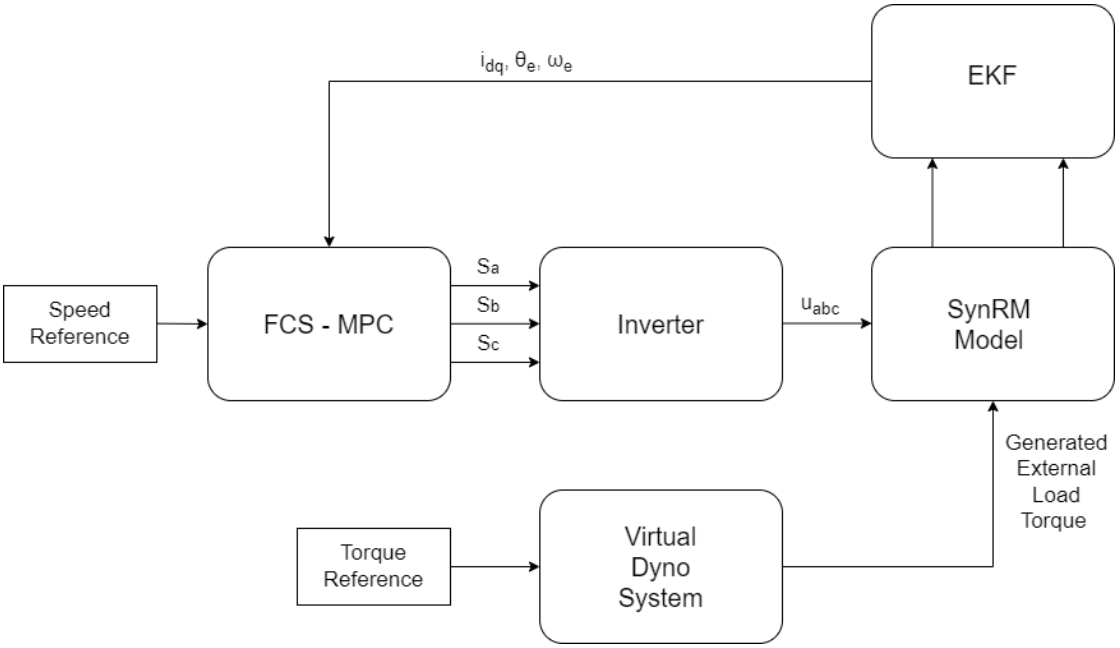

Figure 4.1: Structure of the Virtual Test Bench

4.2 System Setup

The motor and system parameters are listed in Table 4.1 below. The three-phase voltages and currents measured in the SynRM are transformed into the stationary reference frame $\alpha\beta$ as they are the inputs into the EKF to estimate the state variables of the SynRM which are the rotor speed (ω_e), position (θ_e), stator currents (I_{dq}) and load torque (T_L). The estimated variables are fed back into the FOC and FCS-MPC control systems. The value of the sampling time has a great impact on the motor control system, such as the torque and current ripples.
The observer performance is tested over the wide speed range of the machine, and it is also tested under varying load conditions and a brief analysis is done on the effect of the Square Wave Injection signal on the current ripples of the machine. The I_d^{ref} is selected as the rated current of the motor (3A) for both control systems.

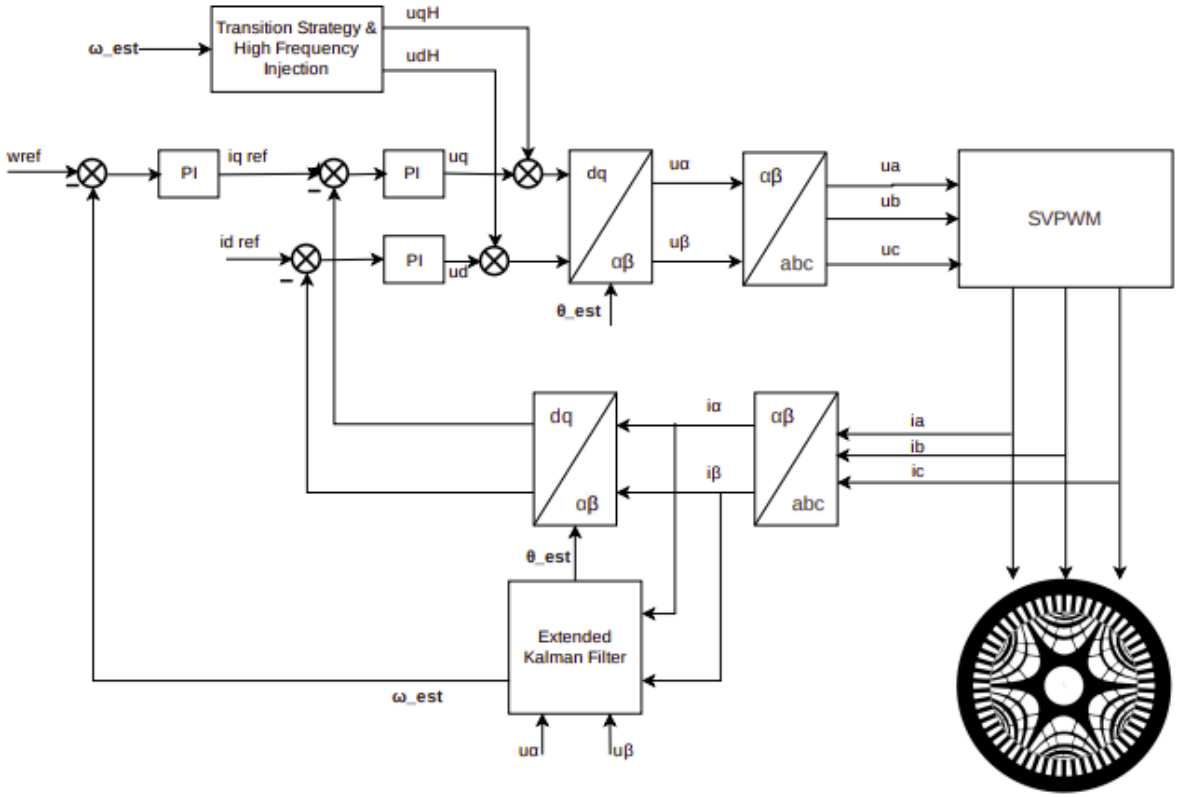

Figure 4.2: Benchmark field-oriented control (FOC) scheme

SynRM Motor Parameters	
Stator Resistance, R_s	0.7198Ω
d-axis Inductance, L_d	0.2607H
q-axis Inductance, L_q	0.0797H
Pole pairs, P	2
Rated Current, I_s	3A
Base Rated Speed [rpm]	1500
Motor Inertia, J	$3.6{*}10^{-3} kgm^2$
Two-level VSI Model	
Switching frequency, f_{sw}	$\frac{f_s}{6}$
DC Voltage, V_{dc}	400V
FCS-MPC Controller Parameters	
Sampling Frequency, f_s	60 kHz
Prediction Horizon, N_p	1
λ_ω	150.23
λ_{T_e}	1.65
λ_{hf}	207.63
FOC Controller Parameters	
K_p^{speed}	0.4
K_i^{speed}	5
K_p^{id}	14.25
K_i^{id}	268.61
K_p^{iq}	14.25
K_i^{iq}	268.61
EKF Parameters	
Process Noise Covariance, Q	diag(0.005,0.0843, 259.388, 3.231e-4, 3.9338)
Measurement Noise Covariance, R	diag(0.0789, 0.0741)

Table 4.1: System Parameters

4.3 Operation Scenarios

There are three simulation scenarios explored: Low, Medium-to-Base and Transition Speed scenarios. Table 4.2 presents the three operation scenarios are presented.

Scenario	Description
1	Low Speed Operation (rpm) : 0-150
2	Medium-to-Base Speed Operation (rpm) : 500-1300
3	Transition Speed Operation (rpm) : 50-1000

Table 4.2: Simulation Scenarios

The two-level VSI operated under SVPWM for the FOC scheme changes its switching states six times during one sampling interval, while the two-level VSI used for the FCS-MPC only changes its switching states once at each sampling interval. Therefore, for the FCS-MPC control scheme, the equivalent switching frequency of the inverter is 1/6 of the FCS-MPC sampling frequency. To make the switching losses performance comparable between the FOC and FCS-MPC control schemes, the default configuration of the FCS-MPC is set to operate at $f_s = 60$ kHz and $N_p = 1$.

4.4 Comparison between FCS-MPC and FOC Controller:

This section focuses on the comparisons of the operation performances between the FCS-MPC and FOC control schemes. The performance of the observer is evaluated in varying operating regions in conjunction with the control schemes with the injection of a 20V square wave voltage signal to the v_d axis of the machine. The average root mean square (RMS) error of the speed is the primary performance objective.

4.4.1 Low Speed Test:

Figures 4.3 and 4.4 show the simulation results of the EKF estimation capacity of speed, position of the rotor, stator currents I_{dq} and load torque in regions of zero and low speed. In figure 4.3, at the starting point, a reference speed of 0 rpm was given. After 0.5 seconds, a step speed of 100 rpm was given to the reference speed. The EKF with both FCS-MPC and FOC showed sufficient dynamic results with injection of square-wave HF signals into the machine terminals, as it accurately estimates the speed and step torque induced in the machine in figure 4.3. The estimation errors of the machine states converge to zero quickly.
The results with the FCS-MPC are better than the results from the FOC in the low speed test. The FCS-MPC has a much faster response than the FOC scheme with minimal overshoot while sufficiently tracking the speed reference, and current references in figure 4.3. The FCS-MPC takes 0.034 seconds to track the current on the d axis I_d and settles much faster than the FOC scheme. This same pattern occurs in the speed tracking, q-axis current tracking.

Cases	RMS error (rpm)	Overshoot	Settling Time (seconds)
FCS at 0 rpm	0.0040	No	0.1
FOC at 0 rpm	0.0587	Yes	0.3
FCS at 100 rpm	2.2934	No	0.1
FOC at 100 rpm	3.5912	Yes	0.45

Table 4.3: Low Speed Test Results

In Figure 4.4, at the starting point, the virtual dyno applies a reference speed of 100 rpm was given. A reference load torque of 0.5 Nm on the machine at 0.25 seconds. The FCS-MPC algorithm showed very good dynamic and steady state performance, and the EKF accurately tracks the load torque induced on the machine.

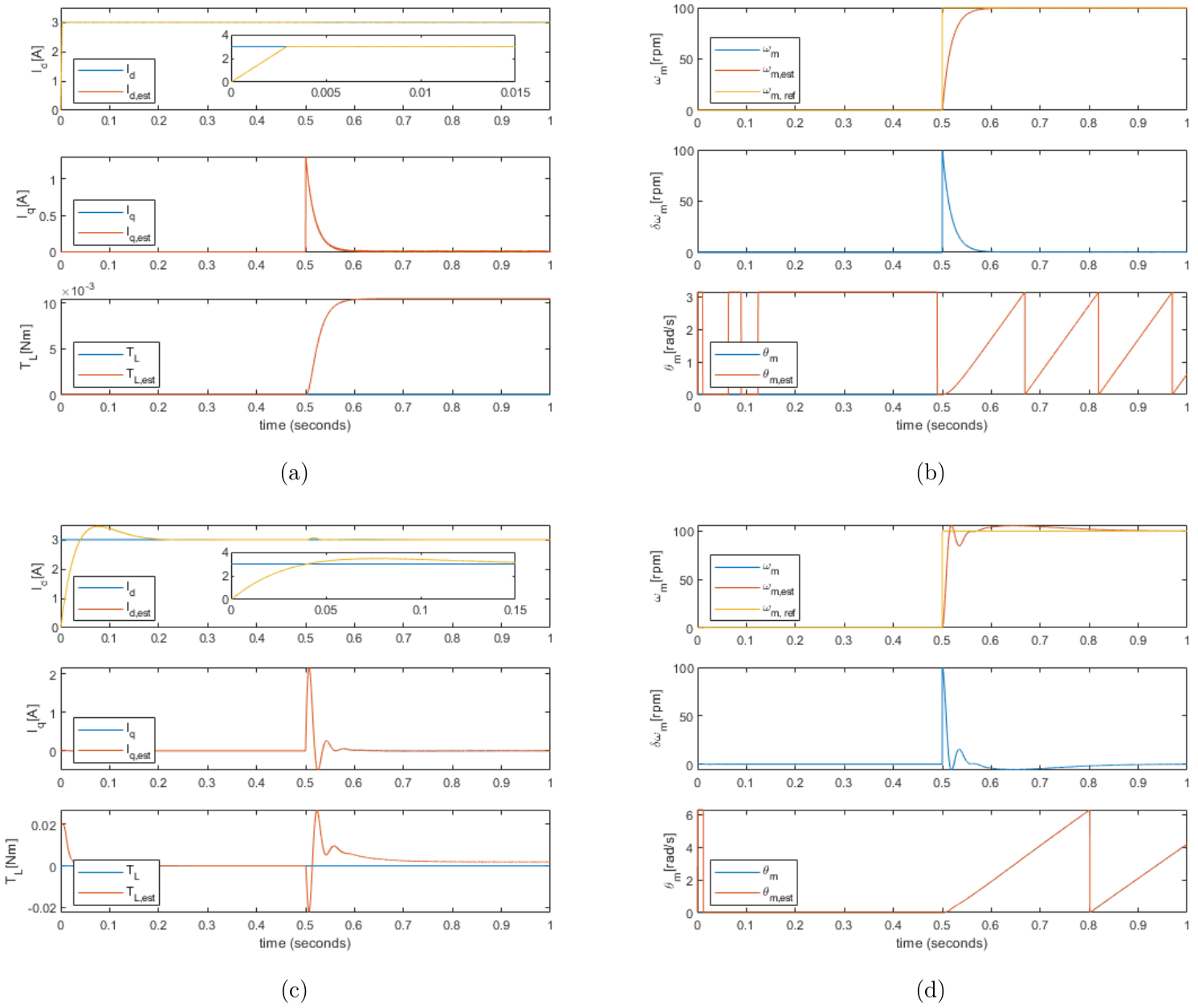

Figure 4.3: Low Speed Performance, (a) FCS - MPC: Actual and estimated currents in dq and mechanical load torque and its estimate, (b) FCS - MPC : Actual and estimated speed, speed error, and estimated, actual rotor position, (c) FOC: Actual and estimated currents in dq and mechanical load torque and its estimate , (d) FOC: Actual and estimated speed, speed error, and actual and estimated rotor position

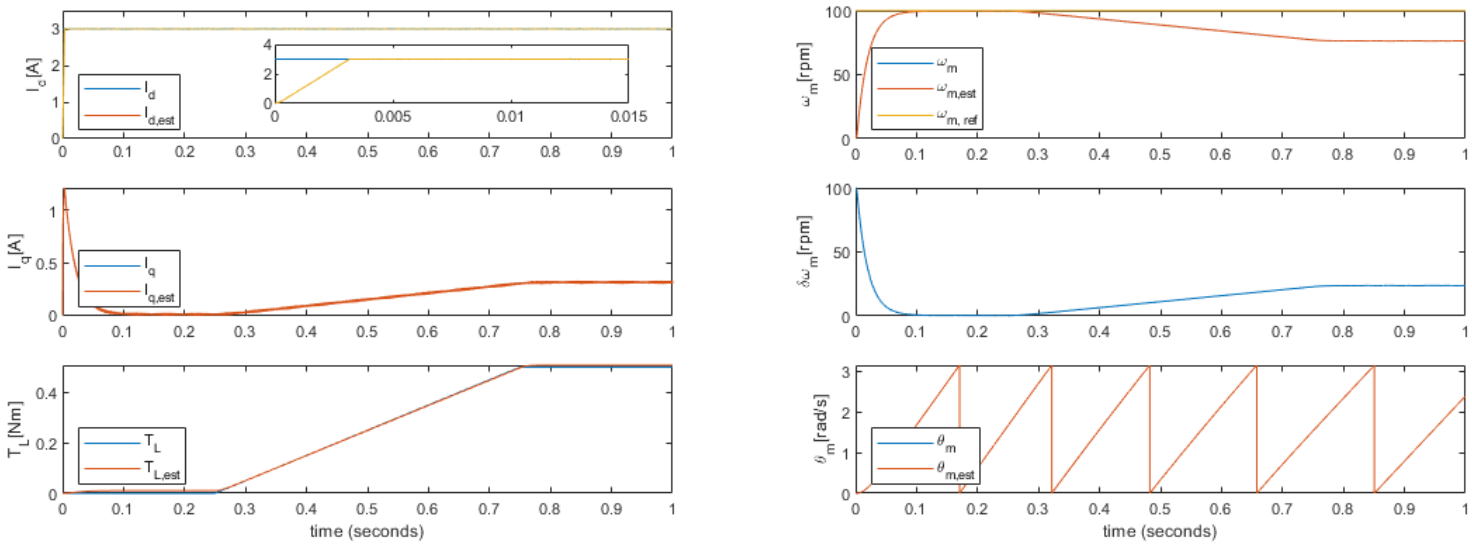

(a) (b)

Figure 4.4: Low Speed Performance, (a) FCS - MPC: Actual and estimated currents in dq and mechanical load torque and its estimate, (b) FCS - MPC : Actual and estimated speed, speed error, and actual and estimated rotor position

4.4.2 Spectral Content of I_d with High Frequency Injection

The spectral content of the phase currents a,b,c is evaluated on the rotary reference frame dq. The EKF does a very good job of filtering out the high-frequency contents produced from the induced voltage signals, resulting in low total harmonic distortions, decreased noise, and decreased switching losses in the inverter.

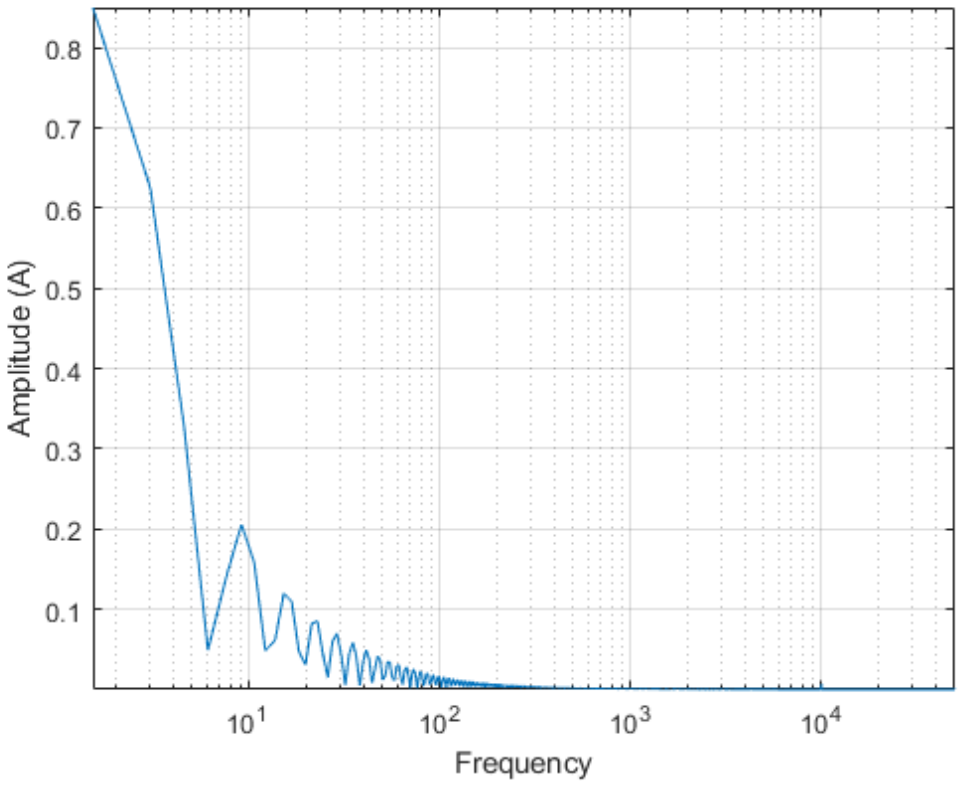

Figure 4.5: Amplitude Spectrum of I_d

4.4.3 Medium-to-Base Speed Performance:

Figures 4.6 show the simulation results of the estimation capability of EKF of the speed, position of the rotor, stator currents I_{dq} and load torque in the medium speed regions.

In figure 4.6, at the starting point, The virtual dyno applies a reference speed of 500 rpm was given. After 0.5 seconds, a 1000 rpm step was given to the reference speed. A reference load torque of 0.5 Nm on the machine at 0.25 seconds. The EKF with both the FCS-MPC and the FOC showed sufficient dynamic results as it accurately drives the rotor speed to the reference speed as can be seen in Figure 4.6. The FCS-MPC algorithm showed very good dynamic and steady state performance compared to the FOC algorithm, with a much lower rms error and minimal overshoot in the speed of the machine. The FOC algorithm and the observer performance showed good steady and dynamic performance with sufficient estimation accuracy, and the position and speed error converge to zero quickly. The current error estimates I_q and I_d quickly converge to zero. This is shown in Figure 4.6 and table 4.4.

From table 4.4, the results with the FCS-MPC are better than the results from the FOC in the medium speed test. The FCS-MPC takes 0.12 seconds to drive the rotor speed of the machine to the reference with no overshoot and it takes FOC 0.35s with acceptable overshoot to successfully drive the speed to the reference speed. The FCS-MPC has a much lower RMS speed error than the FOC scheme with minimal overshoot while sufficiently tracking the speed reference and current references in Figure 4.6.

Cases	RMS error (rpm)	Overshoot	Settling Time (seconds)
FCS at 500 rpm	12.3157	No	0.1
FOC at 500 rpm	16.5898	Yes	0.3
FCS at 1000 rpm	14.9157	No	0.1
FOC at 1000 rpm	22.5114	Yes	0.45

Table 4.4: Medium-to-Base Speed Test Results

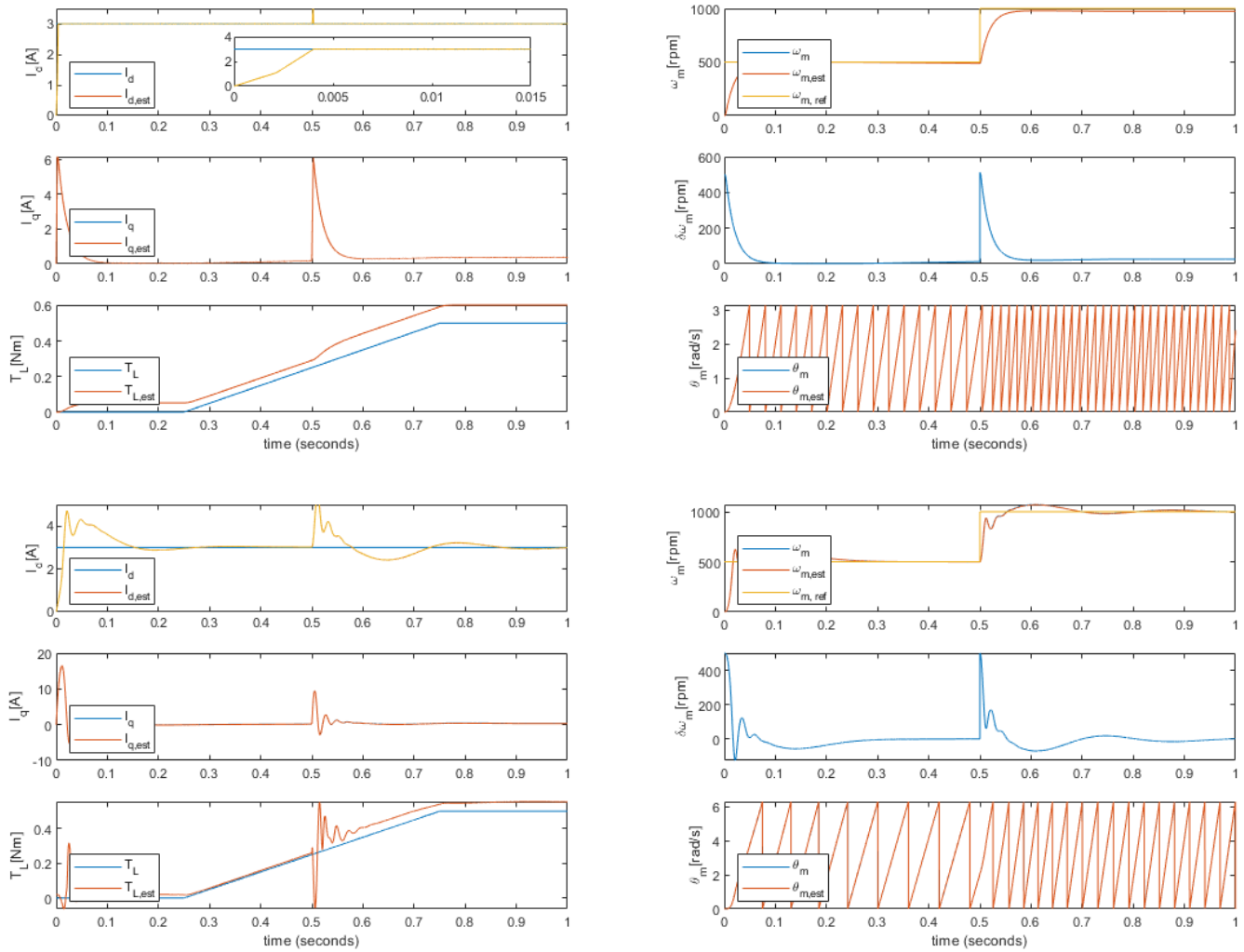

(a) (b)

Figure 4.6: Medium to Base Speed Performance, (a) FCS - MPC: Actual and estimated currents in dq and mechanical load torque and its estimate, (b) FCS - MPC : Actual and estimated speed, speed error, and actual and estimated rotor position, (c) FOC: Actual and estimated currents in dq and mechanical load torque and its estimate , (d) FOC: Actual and estimated speed, speed error, and actual and estimated rotor position

4.5 Transition Performance between Low and Base Speed Region: FCS-MPC

With the simple relational logic expressed in Algorithm 2 to activate the injection of the high-frequency injection signal into the machine terminals for EKF to observe signals in the low-speed regions, the transition performance between the low- and base-speed regions is evaluated to ensure smooth operation and adequate observer performance. Figure 4.7 shows the simulation results of the estimation capability of EKF of the speed, position of the rotor and the operation of the HF injection scheme. An increasing reference speed starting from 50 rpm up to 1000 rpm is given as the input to the system. The EKF with the FCS-MPC showed very good dynamic performance with the injection of HF square wave signals into the terminals of the machine, as it accurately estimates the speed induced on the machine in Figure 4.7. The operation of the HF injection algorithm clearly shows that when the speed is above 150 rpm, no signals are injected in the terminals and it is a smooth transition operation between the low and base speed regions.
The simulation results from this chapter clearly show that the FCS-MPC with EKF has better steady state and dynamic performance in the wide speed range from zero to the base speed of the SynRM than the benchmark FOC system.

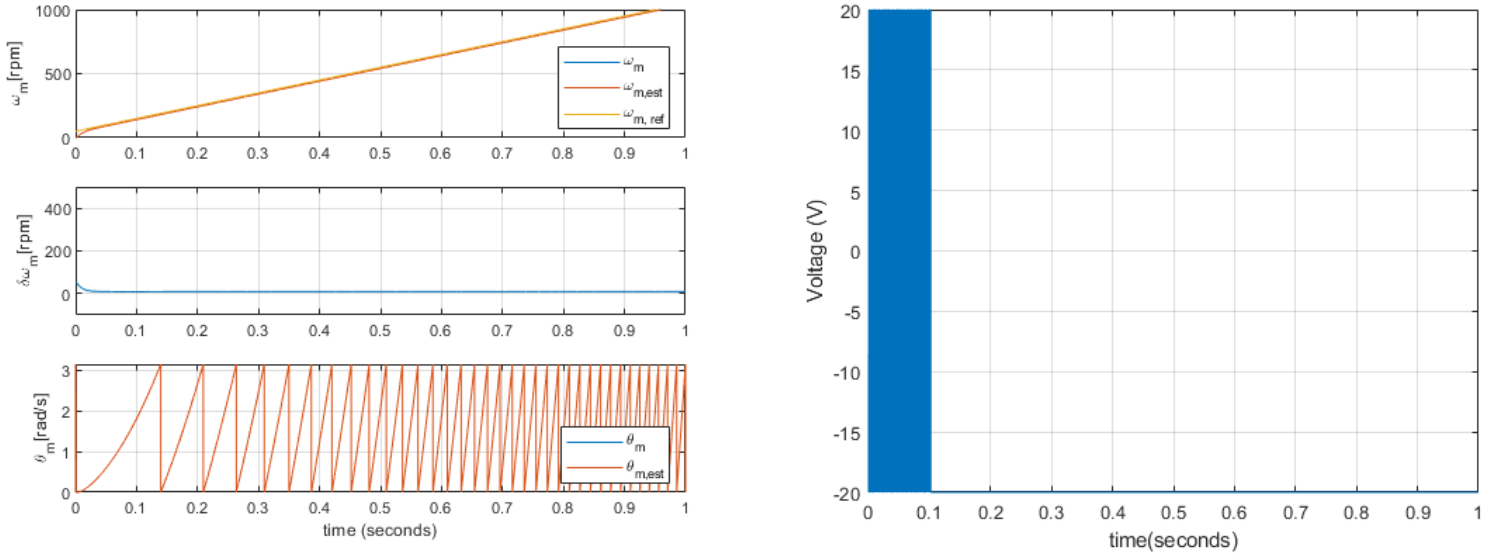

(a) (b)

Figure 4.7: Transition performance, (a) FCS - MPC: Actual and estimated currents in dq and mechanical load torque and its estimate, (b) FCS - MPC : Actual and estimated speed, speed error, and actual and estimated rotor position, (c) FOC: Actual and estimated currents in dq and mechanical load torque and its estimate , (d) FOC: Actual and estimated speed, speed error, and actual and estimated rotor position

Chapter 5

Conclusion and Future Work

5.1 Conclusion

In this report, a simple salient-pole SynRM model is derived based on electrical and mechanical dynamic equations. A literature review of existing control and estimation strategies for sensorless control was conducted.
A Finite Control Set Model Predictive Control has been developed to realize the controller objectives for the SynRM such as speed reference tracking, torque per ampere optimization, and current magnitude limitation. A two-level VSI which only changes its switching states once during one sampling interval is utilized to generate the desired voltage vector for the SynRM. By directly optimizing the 8 possible inverter switching states combined with the discretized SynRM model,the future system states are predicted until the prediction horizon is reached. The optimal switching state for the next time step is evaluated by the cost function.
To execute the FCS-MPC strategy, signals of the position of the rotor, the speed of the rotor, the stator currents in the dq frame and the load torque are required for the prediction model. Classically, this is achieved using position encoders and sensors, which increase the overall cost and noise and decrease the reliability of the system. An extended Kalman Filter was developed, which with the addition of High Frequency Injection Voltage signals applied to the stator of the machine in the low speed regions, was used to estimate these unmeasureable signals without the sensors using the voltage and current information of the machine and the dynamic equations in the $\alpha\beta$ frame which increases the robustness and reliability

of the system. Particle Swarm Optimization is used to tune the weights of the cost function of the controller and the EKF covariance matrices in order to decrease the time taken instead of the trial and error method, which can be time consuming. The performance of the FCS-MPC and EKF was evaluated in different operating regions with different speeds. A given benchmark FOC controller and EKF with a two-level VSI using SVPWM is used to compare the differences between these two control schemes. The FCS-MPC has a better performance with no overshoot and lower settling time when it is compared to the FOC in the wide speed range. The estimation of the angular position and speed at zero and low speed was achieved with good performance with the injection of high frequency voltage signals which is essential particularly if the motor has high inertia or zero position holding is an important application requirement. At up to base speed, the observer provided very good performance without the use of the high frequency injection signals to estimate the angular position and speed of the motor. Hence the aim of designing a single observer for the whole speed range of a SynRM is achieved with the high frequency injection voltage signals turned off and on based on the current speed estimates.

5.2 Future Work

This project report focuses on the realization of the FCS-MPC for a parameter-varying SynRM model. In future work, several aspects can be explored such as:

- A physics based model of the SynRM accounting for magnetic saturation and temperature variation can be developed for the FCS-MPC scheme.
- To account for machine degradation and parameter uncertainties like stator resistance and dq stator inductances, the extended Kalman filter can be extended to estimate these parameters which further improve the robustness and reliability of the estimation strategy. However, the weakness of the filter is in the design and tuning of the process and noise covariance matrices and swarm based optimization algorithms can be used to find the near optimal covariance matrices.

- Evaluation of the Unscented Kalman Filter as an alternative to the extended Kalman filter for nonlinear estimation of dynamical systems. As the unscented Kalman Filter (UKF) is a more efficient nonlinear stochastic filter with computational power similar to the extended Kalman Filter and the SynRM is a highly nonlinear system, the UKF provides an intriguing solution to the sensorless control problem.

- Additional cost functions to improve the FCS-MPC to explore its performance above the base speed region using field-weakening methods such as MTPV.

- Evaluation of the influence on the sampling frequency of the FCS-MPC on the dynamic performance of the machine and the impact of the use of longer prediction horizons N_p, on the system.

- Evaluation of the CCS-MPC as an alternative to the FCS-MPC for MPC of electric drives.

References

[1] C. J. V. Filho, D. Xiao, R. P. Vieira, and A. Emadi, "Observers for high-speed sensorless pmsm drives: Design methods, tuning challenges and future trends," in *IEEE Access*, vol. 9, 2021, pp. 56 397–56 415.

[2] P. Karamanakos and T. Geyer, "Guidelines for the design of finite control set model predictive controllers," in *IEEE Transactions on Power Electronics*, vol. 35, no. 7, 2020, pp. 7434–7450.

[3] B. Bose, *Modern Power Electronics and AC Drives*. Prentice Hall, 2001, pp. 439–530.

[4] P. Cortes, M. P. Kazmierkowski, R. M. Kennel, D. E. Quevedo, and J. Rodriguez, "Predictive control in power electronics and drives," in *IEEE Transactions on Industrial Electronics*, vol. 55, no. 12, 2008, pp. 4312–4324.

[5] F. Briz, J. Cancelas, and A. Diez, "Speed measurement using rotary encoders for high performance ac drives," in *Proceedings of IECON'94 - 20th Annual Conference of IEEE Industrial Electronics*, vol. 1, 1994, pp. 538–542.

[6] R. Petrella, M. Tursini, L. Peretti, and M. Zigliotto, "Speed measurement algorithms for low-resolution incremental encoder equipped drives: a comparative analysis," in *2007 International Aegean Conference on Electrical Machines and Power Electronics*, 2007, pp. 780–787.

[7] M. Konghirun, "A resolver-based vector control drive of permanent magnet synchronous motor on a fixed-point digital signal processor," in *2004 IEEE Region 10 Conference TENCON 2004.*, vol. 4, 2004, pp. 167–170.

[8] S. Jung, B. Lee, and K. Nam, "Pmsm control based on edge field measurements by hall sensors," in *2010 Twenty-Fifth Annual IEEE Applied Power Electronics Conference and Exposition (APEC)*, 2010, pp. 2002–2006.

[9] G. Wang, M. Valla, and J. Solsona, "Position sensorless permanent magnet synchronous machine drives—a review," in *IEEE Transactions on Industrial Electronics*, vol. 67, no. 7, 2020, pp. 5830–5842.

[10] G. Wang, G. Zhang, and D. Xu, *Position Sensorless Control Techniques for Permanent Magnet Synchronous Machine Drives*. Springer, 2020.

[11] Y. Zhang, Z. Zhao, T. Lu, L. Yuan, W. Xu, and J. Zhu, "A comparative study of Luenberger observer, sliding mode observer and extended Kalman filter for sensorless vector control of induction motor drives," in *2009 IEEE Energy Conversion Congress and Exposition*, 2009, pp. 2466–2473.

[12] F. P. Scalcon, C. J. Volpato, T. Lazzari, T. S. Gabbi, R. P. Vieira, and H. A. Gründling, "Sensorless Control of a SynRM Drive Based on a Luenberger Observer with an Extended EMF Model," in *IECON 2019 - 45th Annual Conference of the IEEE Industrial Electronics Society*, vol. 1, 2019, pp. 1333–1338.

[13] Q. Li, R. Li, K. Ji, and W. Dai, "Kalman filter and its application," in *2015 8th International Conference on Intelligent Networks and Intelligent Systems (ICINIS)*, 2015, pp. 74–77.

[14] C. Moon, K. H. Nam, M. K. Jung, C. H. Chae, and Y. A. Kwon, "Sensorless speed control of permanent magnet synchronous motor using Unscented Kalman Filter," in *2012 Proceedings of SICE Annual Conference (SICE)*, 2012, pp. 2018–2023.

[15] V. Šmídl and Z. Peroutka, "Marginalized pinproceedings filter for sensorless control of pmsm drives," in *IECON 2012 - 38th Annual Conference on IEEE Industrial Electronics Society*, 2012, pp. 1877–1882.

[16] K. C. N. Sridivya and T. V. Kiran, "Space vector pwm control of bldc motor," in *2017 International Conference on Power and Embedded Drive Control (ICPEDC)*, 2017, pp. 71–78.

[17] J. Rodriguez and P. Cortes, *Predictive Control of Permanent Magnet Synchronous Motors*. Wiley-IEEE Press, 2012, pp. 133–144.

[18] F. Toso, P. G. Carlet, A. Favato, and S. Bolognani, "On-line continuous control set mpc for pmsm drives current loops at high sampling rate using qpoases," in *2019 IEEE Energy Conversion Congress and Exposition (ECCE)*, 2019, pp. 6615–6620.

[19] A. Farhan, M. Abdelrahem, A. Saleh, A. Shaltout, and R. Kennel, "Robust sensorless direct speed predictive control of synchronous reluctance motor," in *2020 IEEE 29th International Symposium on Industrial Electronics (ISIE)*, 2020, pp. 1541–1546.

[20] T.-H. Liu, H. Haslim, and S.-K. Tseng, "Predictive controller design for a high-frequency injection sensorless synchronous reluctance drive system," in *IET Electric Power Applications*, vol. 11, 2016.

[21] R. Caro, C. A. Silva, R. Pérez, and J. I. Yuz, "Sensorless control of a synrm for the whole speed range based on a nonlinear observability analysis," in *2017 IEEE International Conference on Industrial Technology (ICIT)*, 2017, pp. 336–341.

[22] N. Kaur and A. Kaur, "A review on tuning of extended kalman filter using optimization techniques for state estimation," in *International booktitle of Computer Applications*, vol. 145, 2016, pp. 1–5.

[23] W. F. W. Tarmizi, I. Elamvazuthi, N. Perumal, K. Nurhanim, M. A. Khan, S. Parasuraman, and A. Nandedkar, "A particle swarm optimization-pid controller of a dc servomotor for multi-fingered robot hand," in *2016 2nd IEEE International Symposium on Robotics and Manufacturing Automation (ROMA)*, 2016, pp. 1–6.